High-frequency *P* and *S* velocity anomalies in the upper mantle beneath Asia from inversion of worldwide traveltime data

Ivan Koulakov[1]

Received 18 August 2010; revised 24 December 2010; accepted 10 January 2011; published 5 April 2011.

[1] A model of seismic *P* and *S* anomalies in the upper mantle beneath Asia (in limits of 35°E–140°E, 12°N–57°N) was constructed based on the tomographic inversion of traveltime data from the revised ISC catalog for the years 1964–2004. The inversions were performed independently in 32 overlapping circular windows that cover the entire study area. The free inversion parameters in each window were defined individually depending on the available data based on synthetic modeling. Such adaptive tuning of parameters enables more optimal usage of the input data in areas with inhomogeneous ray coverage compared to global inversions. This approach resolves high-frequency patterns but is less sensitive to large anomalies with sizes comparable to the window diameter. Thus, this approach is somewhat similar to high-frequency filtration of the velocity distribution. The resolution capacity of the model was tested using checkerboard tests with various pattern sizes. To assess the role of random noise, independent test inversions of two data subsets (with odd and even numbers of events) were performed. Clear reconstructions of known structures, such as subducting plates beneath the Japan and Ryukyu arcs whose locations and shapes have been constrained by other studies, further indicate the reliability of the model. The 3-D models of *P* and *S* anomalies presented in horizontal and vertical sections show complex interactions of the lithospheric segments beneath the Alpine-Himalayan orogenic belts. Particular attention is focused on the collisional areas of Iran, Pamir-Hindukush, Tien-Shan, and Burma. The digital version of the 3-D *P* and *S* models is available at http://www.ivan-art.com/science/REGIONAL.

Citation: Koulakov, I. (2011), High-frequency *P* and *S* velocity anomalies in the upper mantle beneath Asia from inversion of worldwide traveltime data, *J. Geophys. Res.*, *116*, B04301, doi:10.1029/2010JB007938.

1. Introduction

[2] The tectonics of Asia are extremely complex, with collisional processes [e.g., *Molnar and Tapponnier*, 1975] coexisting with rifting and recent intracontinental volcanic activity [e.g., *Zonenshain and Savostin*, 1981]. Many important questions related to lithospheric interactions in Asia are actively debated, and addressing these questions requires more quantitative information on the deep structure of the lithosphere. One of the most debated topics concerns the mechanism of recycling of the continental lithosphere in areas of continent-continent collisions. Southern Asia is affected by the northward drift of the Indian and Arabian continents. Closing of the ocean basins between the two continents, as well as related oceanic subduction, ended more than 50 million years ago [e.g., *de Sigoyer et al.*, 2000; *Clift et al.*, 2002]. Since then, up to 1,500 km of continental shortening has occurred [e.g., *Replumaz et al.*, 2004]. This resulted in the coupling of crust and mountain building along the entire Alpine-Himalayan orogenic belt. However, the fate of the mantle portion of continental lithosphere in the shortened areas is still an open question. Did it subduct like oceanic lithosphere? Is the continental lithosphere dense enough to sink? The thick lithosphere in cratonic Precambrian blocks appears to be buoyant and does not sink [e.g., *Boyd*, 1989; *Jordan*, 1978]. However, in a continent-continent collision, the transitional, not cratonic, lithosphere may be denser than the underlying asthenosphere, which causes Raleigh-Taylor instability and subduction-like processes. If this is the case, why do we not observe continuous penetration of the lithosphere into the mantle beneath such collision areas in tomographic models of continent-continent collisions (e.g., *Bijwaard et al.* [1998] and this study)?

[3] Answering these and other questions requires robust and reliable information about the deep crustal structure. For Europe, thanks to a large amount of high-quality data and independent studies, many mutually consistent results have been obtained [e.g., *Bijwaard et al.*, 1998; *Piromallo and Morelli*, 2003; *Koulakov et al.*, 2009]. These tomographic models have deciphered the complex structure beneath Europe and have unambiguously answered many geodynamical questions.

[1]Institute of Petroleum Geology and Geophysics, SB RAS, Novosibirsk, Russia.

0148-0227/11/2010JB007938

[4] In Asia, the situation is much more difficult. Dozens of papers describing different seismic models of the mantle structure beneath Asia have been published over the last several decades. Most of the regional upper mantle models of Asia have been obtained using surface wave data, as they provide more uniform ray sampling [e.g., *Curtis et al.*, 1998; *Griot et al.*, 1998; *Wu et al.*, 1997; *Ritzwoller and Levshin*, 1998; *Villaseñor et al.*, 2001; *Friederich*, 2003; *Priestley et al.*, 2006; *Maggi and Priestley*, 2005; *Kustowski et al.*, 2008]. Global surface wave tomography studies also provide important information about the *S* velocity structure of the upper mantle beneath Asia (*Ekström et al.* [1997], *Ritzwoller et al.* [2002b], and others). The *P* velocity structure beneath Asia has been investigated in large-scale body wave regional tomographic studies [e.g., *Ritzwoller et al.*, 2002a; *Huang and Zhao*, 2006; *Replumaz et al.*, 2010; *Koulakov et al.*, 2002; *Koulakov*, 2008; *Koulakov and Bushenkova*, 2010], as well as derived from global tomographic models [e.g., *Bijwaard et al.*, 1998; *Fukao et al.*, 2003; *Li et al.*, 2008]. These references (which do not cover all the relevant papers on this subject) illustrate the large number of different studies that provide information on the mantle structure beneath Asia. At the same time, comparison of the results in these papers shows that they are often not consistent and even contradictory. These differences are mostly related to problems with the data used in the studies. The coverage of seismic stations in Asia is generally sparse and uneven. Information from some countries is not available, which creates large information gaps. The seismic data quality recorded by Asian stations and collected in international catalogs is usually poorer than that of European stations. The strong discrepancies between different tomographic models show that the problem of studying the deep structure beneath Asia still remains open.

[5] Herein, I present a new model of the upper mantle beneath Asia based on tomographic inversion of body waves from worldwide catalogs. Several arguments to demonstrate the robustness of this model are provided. I then compare the model with existing regional and global models and discuss similar features and differences. Finally, I consider some selected regions in Asia and briefly discuss the geodynamical scenarios for these areas.

2. Data and Algorithm

[6] The traveltimes of *P* and *S* body waves reported by the International Seismological Center [*ISC*, 2001] for the time period from 1964 to 2004 were used as the initial data in this study. The advantage of the ISC data, compared to data from local networks, is their large time span and global coverage. However, the quality of the data provided by the ISC is rather poor due to the presence of numerous outliers and outdated schemes for locating earthquakes. These data require additional preprocessing before being used for tomographic inversions. An important revision of the ISC catalog was done by *Engdahl et al.* [1998], who refined the locations of the clearest worldwide events using more sophisticated location algorithms. However, their criteria for data selection were rather conservative and resulted in considerable reduction of the catalog volume. A number of weak events in areas with moderate tectonic activity were rejected, which enlarged nonilluminated areas where body wave tomography cannot provide robust results.

[7] We performed our own revision of the ISC catalog based on similar approaches as those by *Engdahl et al.* [1998], but we used more liberal criteria for data selection. All events between 1964 and 2004 were localized using the algorithm described by *Koulakov and Sobolev* [2006]. This location algorithm is based on the rays constructed in the 1-D spherical model AK 135 [*Kennett et al.*, 1995]. The traveltimes are then corrected for surface relief, the ellipticity of the Earth, and Moho depth (using the model *CRUST2.0* [*Bassin et al.*, 2000]). The formulas for computing the crustal corrections are those by *Koulakov et al.* [2009]. Furthermore, the depth phases (pP and sS) were used to improve the depth location of the sources. In this algorithm, special attention was paid to the problem of rejecting outliers, which make up a considerable part of the ISC catalog (~25–30%). When reprocessing the ISC catalog, we used only events with an azimuthal GAP of less than 180°. The residuals larger than 4 and 6 s for *P* and *S* data, respectively, were rejected. A minimum of 30 recorded *P* and *S* phases was considered at all available epicentral distances for the events.

[8] The average quality of our source locations cannot compete with the catalog by *Engdahl et al.* [1998] who provided the solutions for only robust events. However, the amount of our data is considerably larger that enabled denser ray coverage in most regions. It is a rather long discussion, what is better for tomography: fewer data with only high-quality locations or a larger data set with less accurate source determinations. In my opinion, tomography is much more sensitive to the ray coverage than to the accuracy of source locations. For example, I have shown in my recent paper [*Koulakov*, 2009a], that in the case of local earthquake tomography, adding out-of-network events, though with significant misfits, crucially improves the resolution of tomographic inversion in the target region. I believe that similarly to the mentioned study, adding some events with erroneous depth locations (within reasonable limits) does not decrease the quality of the regional-scale tomographic inversion and even may improve it thanks to better ray coverage.

[9] In this study, the inversion was performed separately in overlapping circular windows that cover the entire study area (Figure 1). After computing the results in all the areas, they were combined in one model for the entire study area. In total, 32 windows with radii of 8° were used. This window size was based on the work of *Koulakov and Sobolev* [2006], who showed that an optimal ray configuration for upper mantle tomography is achieved when the diameter of the study volume is approximately twice its depth.

[10] When performing inversions for large regions, strong variations of the data coverage usually take place. Using one set of inversion parameters for the entire area may cause nonoptimal damping in areas with poor and/or excessive ray density. By performing the inversion with several windows, the inversion parameters can be tuned separately to achieve the best results in each window.

[11] The properties of the solutions were mainly controlled by smoothing, and its optimal values strongly depend on the amount and distribution of data, as well as on the accuracy of picks. However, it is difficult to formalize these

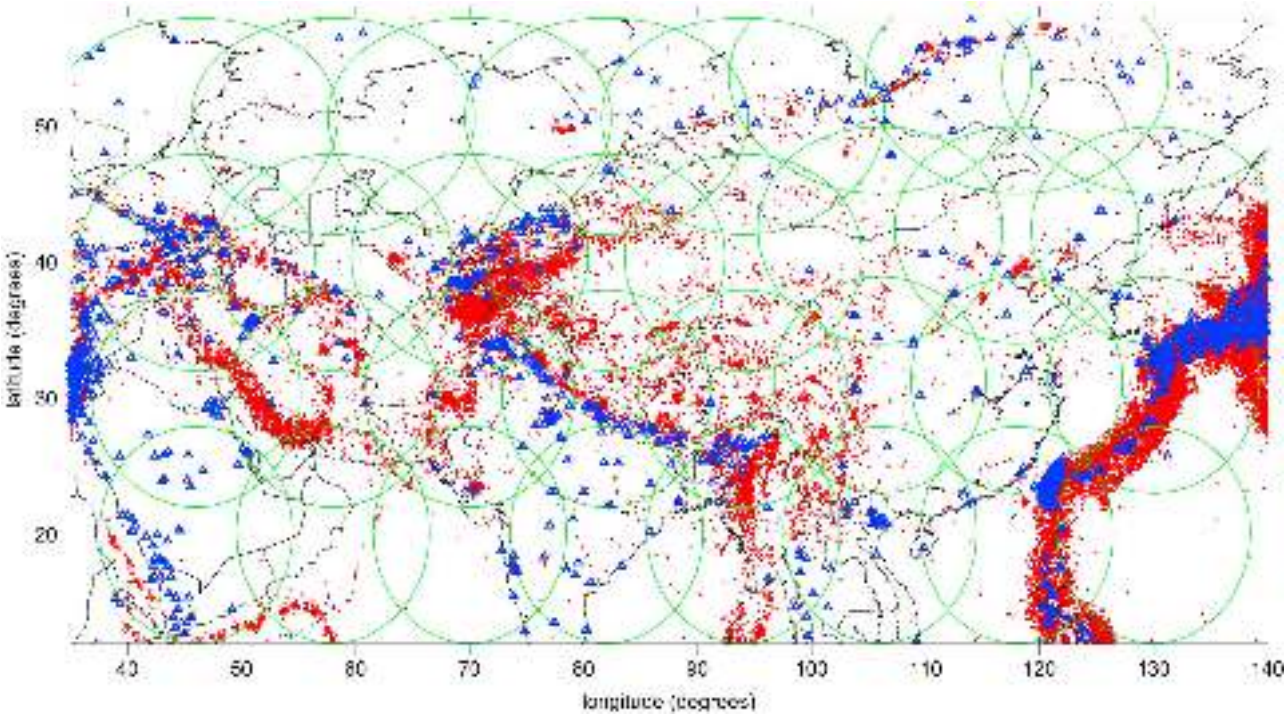

Figure 1. Study area. Blue triangles, seismic stations from the ISC catalog; red dots, relocated seismicity from the catalog used in this study; green circles, locations of 32 areas where the separate inversions were performed.

dependences. The initial smoothing values for each area were derived based on an empirical relationship which determines larger smoothing coefficients for larger data sets. For much noisy *S* data, the smoothing should be two or three times stronger than in the case of *P* data. To achieve better result, the smoothing values were further tuned based on synthetic tests (e.g., checkerboard) with realistic noise. In this case, the best parameters should enable the best resemblance of the reconstructed and synthetic models. The estimated values of *P* and *S* smoothing for each window are shown in Table 1. This selective approach provides a more optimal inversion regime and often resolves higher-frequency patterns than in global inversions. However, it is not sensitive to large anomalies with sizes comparable to, or larger than, the window diameter. Thus, this approach is somewhat similar to high-frequency filtration of the velocity distribution.

[12] Such a step-by-step approach requires more modest computer resources than global inversions; this work was performed on a regular laptop. Furthermore, it provides an opportunity to check the inversion stability in overlapping areas of different windows. On the other hand, in the case of using rays that partly travel outside the current window, patterns in the target area can be biased due to effects of outside anomalies. This problem was investigated in synthetic tests here and in our previous work [e.g., *Koulakov et al.*, 2009], which showed that the algorithm is able to separate the anomalies inside the target area from outside anomalies, which are considered as noncoherent noise. This will be discussed in more detail when describing the results of the synthetic testing.

[13] Two types of data were used for the inversion. One data group included traveltimes from the events located inside the current circular window and recorded by the worldwide stations at all available epicentral distances. This study considered events with a minimum of 30 to 50 phases, depending on the ray coverage in the window. The other data group (direct teleseismic scheme) included the traveltimes corresponding to events located outside the current window and recorded by stations located inside. In this study, the minimum number of stations inside the window that recorded an outside event varied from 25 to 60. The numbers of rays in separate areas, which are given in Table 1, varied from ~7,000 to 700,000, depending on the window. For the entire area, more than 4 million rays were used. The distribution of sources and stations in Asia is shown in Figure 1.

[14] The tomographic inversion is based on a linearized approach. The calculations are performed based on the rays constructed in the 1-D spherical model AK 135 [*Kennett et al.*, 1995], using only one iteration. In principle, it would be possible to adapt nonlinear iterative approaches to this case (for example, the *LOTOS* algorithm developed by *Koulakov* [2009b]), but this would greatly increase the calculation time and would increase the difficulty of accurately tuning the parameters, which requires performing several trials on real and synthetic data. The negative effects of nonlinearity are not very important in this case. Indeed, the expected amplitude of the velocity anomalies in the mantle does not exceed 3–5%. For such amplitudes, the nonlinear effects are small and can be neglected. Even in areas with very strong heterogeneities (e.g., in central Java, with anomalies of 30%

Table 1. Parameters of Windows, Number of events, and Traveltimes According to Two Considered Observation Schemes and Smoothing Coefficients for *P* and *S* Models Used in Inversion in Each Individual Window

Longitude (degrees)	Latitude (degrees)	Radius (degrees)	Regional Events, All Stations		Regional Stations, Teleseismic Events			
			N_events	N_rays	N_events	N_rays	Sm_P	Sm_S
46	20	8	202	14687	510	3742	0.5	1.5
46	30	8	1133	90095	1069	8601	1.4	4.6
46	40	8	1688	129534	8489	89347	1.6	5.2
46	50	8	327	25652	3823	31066	0.8	2.5
58	20	8	522	42677	0	0	1.1	3.0
58	30	8	1837	153054	1520	10464	2.8	7.0
58	40	8	1001	78792	2924	22331	2.2	6.4
58	50	8	50	7470	0	0	0	0
70	20	8	278	16826	420	3013	0.8	2.5
70	30	8	4045	221594	5505	44438	3.3	10.0
70	40	8	5365	277885	11439	108814	3.8	13.1
70	50	8	290	47715	34	205	1.4	4.4
82	20	8	58	5737	1695	12964	0.8	2.0
82	30	8	1297	78142	18500	197694	2.3	5.1
82	40	8	2509	151504	4091	31524	2.8	5.5
82	50	8	534	69731	4821	37719	2.0	5.8
94	20	8	1371	100111	1424	10016	2.5	6.0
94	30	8	1993	137050	7242	51691	2.8	5.5
94	40	8	671	58891	0	0	1.8	6.0
94	50	8	270	24469	3753	26722	1.2	3.5
106	20	8	376	24568	5550	43808	1.2	3.5
106	31	8	728	48513	7094	50781	1.6	4.5
106	42	8	324	23393	7550	53090	1.4	4.0
106	53	8	303	21001	1618	10711	0.8	2.0
118	20	8	6306	343778	3180	27149	3.5	10.0
118	31	8	3087	157433	3915	39636	2.5	7.5
118	42	8	244	15184	9772	77786	1.5	5.0
118	53	8	254	17525	100	680	1.2	4.0
130	20	8	1963	124864	1084	10447	2.8	6.0
130	31	8	11632	623769	9519	156568	5.0	15.0
130	42	8	2753	184422	14060	151790	4.0	11.0
130	53	8	154	13530	241	1890	1.2	4.0

[*Koulakov et al.*, 2007]), using a nonlinear iterative approach does not greatly affect the shapes of the main patterns. In these cases, an underdamped solution with one iteration (linear approach) is nearly identical to an overdamped solution after several iterations.

[15] Parameterization of the velocity fields is performed on the basis of the algorithm developed by *Koulakov* [1998] and *Koulakov et al.* [2002]. A set of nodes is distributed within the study volume according to the ray coverage. In this study, the nodes were placed in 15 horizontal levels at depths of 25, 50, 75, 100, 150, 220, 290, 360, 430, 500, 570, 640, 710, 800, and 900 km. The uppermost level at 25 km is not representative, because in most parts of the study area the rays do not intersect each other at this depth. Therefore, the results at this depth can be considered as station corrections rather than as a true velocity structure. The nodes are distributed on each plane along parallel lines proportional to the ray density. A minimum distance of 30 km is fixed between the nodes in areas with high ray density. The number of nodes in each circular area is about 3,000–9,000 for the *P* model and 2,500–7,000 for the *S* model. Eight nodes control each point of the study area, and the velocity distribution is approximated using a bilinear interpolation. This parameterization might bias the resulting model due to the operator-induced orientations of the lines along which the nodes are distributed. In order to avoid this problem, we performed separate inversions for two different grids, oriented at 0° and 45°. Summation of the resulting models removes most of the artifacts related to the grid orientation.

[16] The first derivative matrix *A*, which reflects the traveltime variation of the *j*th ray due to a unit velocity anomaly at the *i*th node, is computed by integration along the raypaths. Together with the unknown *P* and *S* velocity anomalies, the matrix includes the elements for corrections of the source parameters and station corrections. Source parameters include three coordinate corrections and one time correction for a source located inside the study area, as well as a one-time correction for a remote event. When the stations were located inside and outside the study area, the station corrections were separated.

[17] Smoothing of the resulting velocity anomalies is controlled by an additional matrix block. Each line in this block contains two nonzero elements with opposite signs, corresponding to neighboring nodes in the model. Increasing weights of these elements produces a smoothing effect upon the resulting anomalies. A determination of all the coefficients in the matrix is performed using synthetic modeling for all windows separately.

[18] The resulting matrix is inverted using the LSQR method [*Paige and Saunders*, 1982; *van der Sluis and van der Vorst*, 1987]. The variance reduction for *P* residual times is ~35–40%, while for *S* data it is only ~20–25%. This result demonstrates that the noise level in the *S* traveltimes is significantly higher than in the *P* traveltimes.

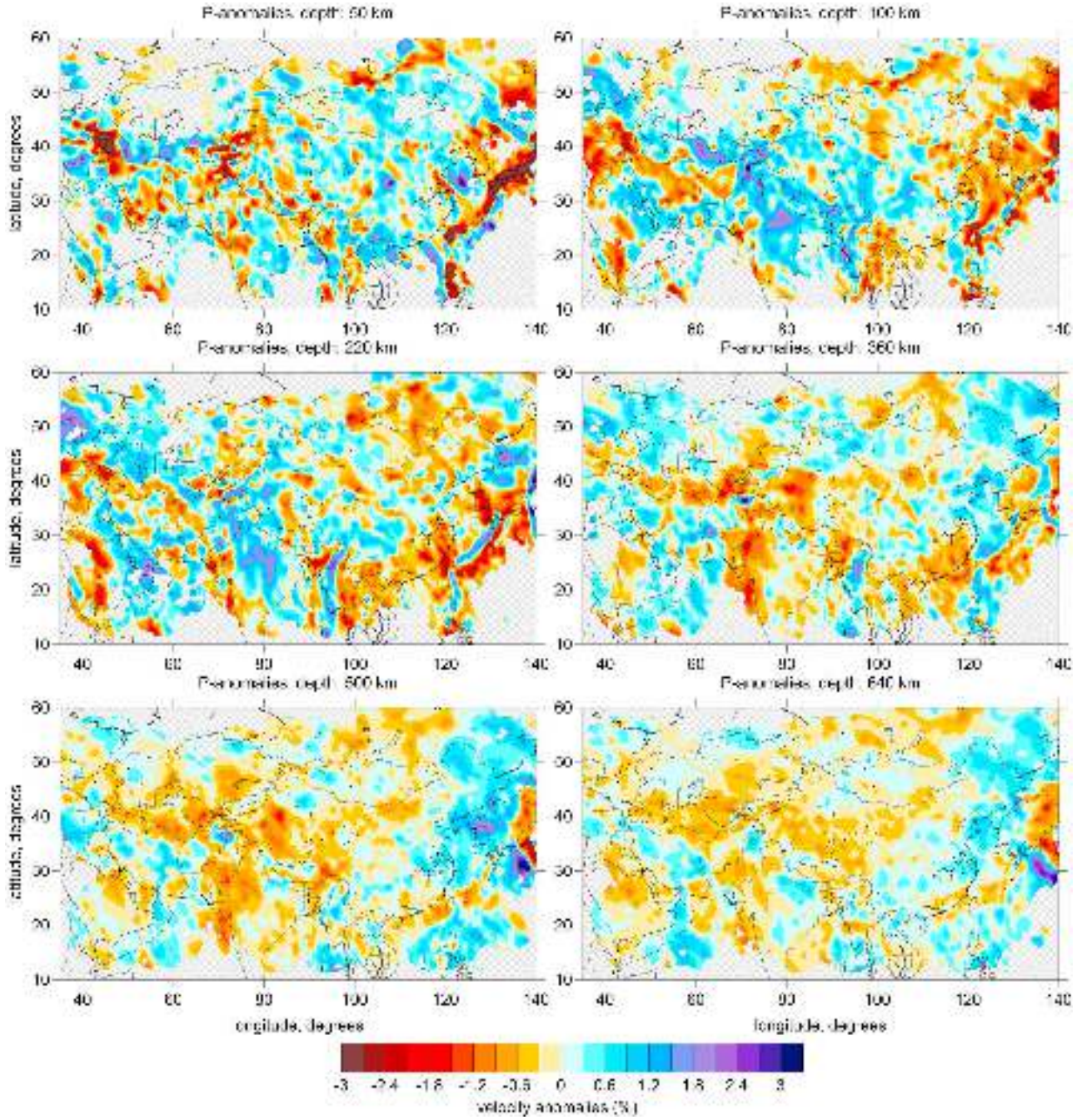

Figure 2. Horizontal sections of *P* velocity anomalies in the upper mantle beneath Asia.

[19] When performing inversion, I used different weighing for source parameters depending on the scheme used. For the sources located inside the study area, separate weights for horizontal and vertical shifts, and for origin times were defined. In cases when I use sources located outside the study area, only time corrections for each source were determined.

[20] The resulting model for the entire area is computed by summation of all results derived for all windows and grids (in this case, two models were computed for each window using differently oriented grids). The summary model is computed as the weighted average:

$$dV^{sum} = \sum_{i=1}^{N} C(d^{cen}) D(d^{node}) dV_i \Big/ \sum_{i=1}^{N} C(d^{cen}) D(d^{node}), \quad (1)$$

where N is the number of models (64, in our case); C is the weight function depending on the distance from the center of the current model (for distances up to R/2, where R is the radius of the current area, $C = 1$; for distances from $R/2$ to R,

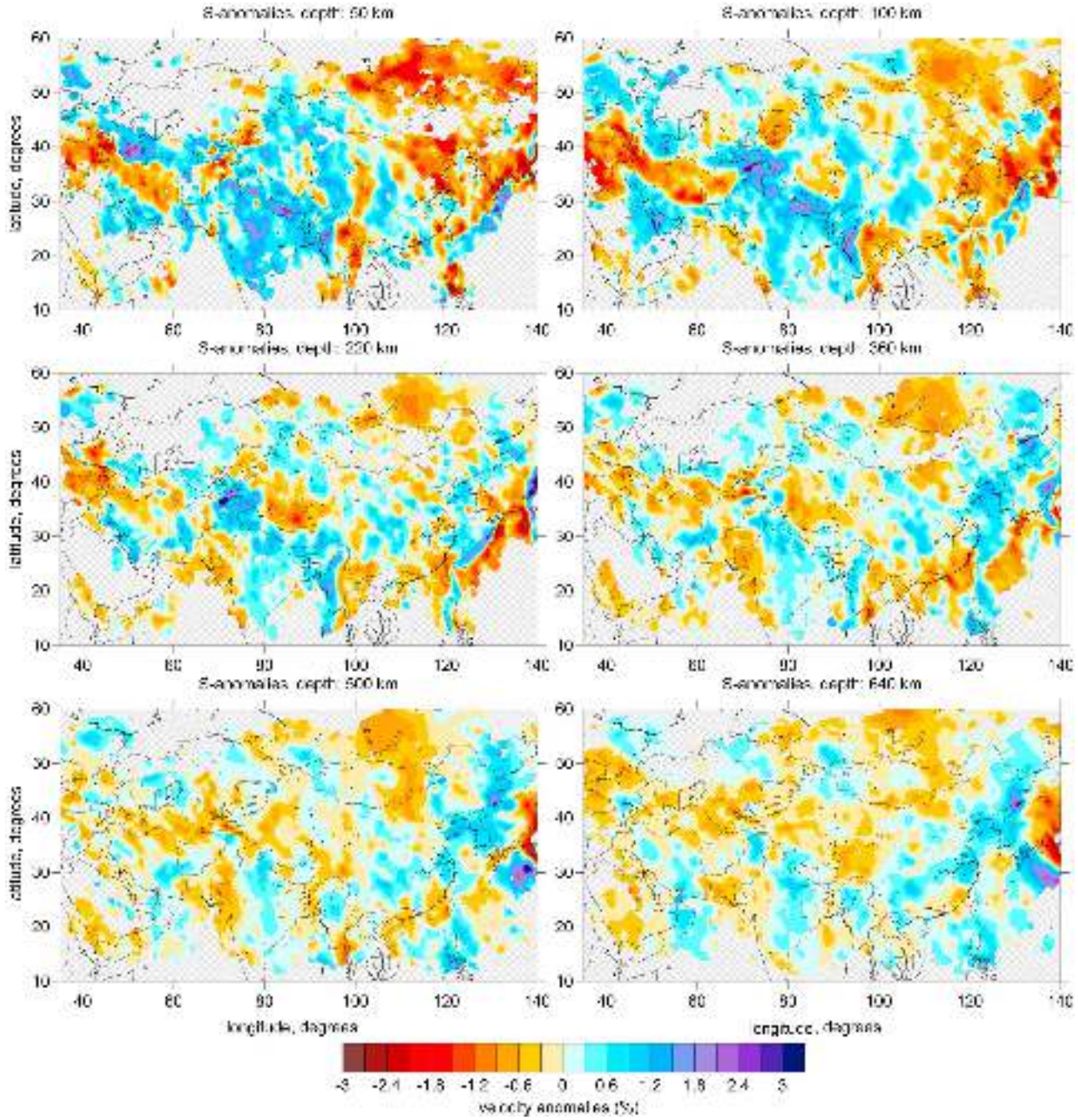

Figure 3. Horizontal sections of *S* velocity anomalies in the upper mantle beneath Asia.

the value of *C* decreases linearly from 1 to 0); *D* depends on the distance to the nearest parameterization node.

3. Results and Verification

[21] The summary models of *P* and *S* velocity anomalies in the upper mantle beneath Asia are presented in six horizontal sections in Figures 2 and 3. In addition, details of the resulting model in several areas are shown in horizontal and vertical sections in section 4. The digital version of the 3-D *P* and *S* models is available online at http://www.ivan-art.com/science/REGIONAL with a simple script that generates horizontal and vertical sections. The resulting anomalies are shown only if the distance to the nearest parameterization node is less than 80 km. For the areas not covered by seismic rays, the nodes are not installed, and the resulting anomalies are shaded. The most important and difficult problem of any tomographic study is to provide objective information about the reliability of the presented patterns. Therefore, before discussing the resulting model, I present some arguments for the degree of reliability of the anomalies obtained in different parts of the study area.

[22] Seismic tomography is still considered to be an imperfect tool that often provides quite different images for same areas. As described in the introduction, some regional and global models of Asia are inconsistent with each other. Therefore, a close correlation between different models constructed using different data and approaches is a strong indication for the robustness of these models. The general structure of the model presented here correlates well with the results of many of the previous studies mentioned in the introduction. For example, the *S* velocity models by *Bijwaard et al.* [1998] and *Villaseñor et al.* [2001] are very well correlated with the results of this study (e.g., our result at 100 km depth (Figure 3) reproduces almost all the details of the model shown by *Villaseñor et al.* [2001, Figure 9b]). There are rather good correlations of the *P* and *S* anomalies at 50 km depth in this model with the Pn and Sn velocities presented by *Ritzwoller et al.* [2002]. The *P* velocity model in this study can also be compared with global models, such as those by *Bijwaard et al.* [1998] and *Li et al.* [2007]. In shallower sections (above 300 km depth), all these models differ considerably. However, a smoothed version of the model in this study is similar to that of *Bijwaard et al.* [1998]. Further smoothing and bias of the reference level will make it more similar to the model by *Li et al.* [2007]. At greater depths, the models provide more consistent structures.

[23] The reliability of the results can be demonstrated by revealing a structure with known a priori patterns that have been identified by reliable independent sources. Subducting oceanic slabs are some of the clearest features in the mantle, and are robustly defined in most tomographic models as high-velocity patterns. The model in this study includes, on its eastern side, a portion of the Ryukyu and Japan arcs, where oceanic subduction zones are present. The high-velocity slab that coincides with the Benioff seismicity is clearly observed and fits with other tomographic models [e.g., *Bijwaard et al.*, 1998]. Note that for the Ryukyu arc, the station distribution is rather poor, and the model is derived mostly on the basis of events recorded by world-wide stations, similar to many other parts of Asia. The algorithm provides reasonable results for these well-known structures, which gives us confidence in the results in other parts of the model.

[24] To check the robustness of the results, the role of random noise in the data and the resolution of the derived model must be evaluated. The low variance reduction in the inversion (from 25 to 40%) shows that the noise level in the data is significant. Reconstruction with independent data subsets is a test that allows the estimation of the bias of the results due to random noise. This test implies a random separation of the entire data set into two groups (e.g., with odd and even numbers of events) and their independent inversions. The processing algorithm and free parameters for the grid construction and inversion are the same as in the case of the inversion of the entire data set.

[25] The inversion results for the halved *P* and *S* data sets are shown in Figure 4. These models can be compared with each other and also with the results obtained using the entire data set (Figures 2 and 3) to demonstrate the effect of halving the data on the inversion results. It is worth noting that reducing the data by half increases the role of the additional smoothing matrix block that is used for the inversion damping. This leads to smoother solutions for the halved data sets compared to the main result.

[26] It can be observed that the *P* and *S* models show a good correlation of the general patterns at corresponding depths. However, some details are quite different. The degree of inconsistency varies considerably in different regions and is controlled by amount and quality of the data provided by the regional networks. Features that appear different on the odd and even tests may be artifacts related to noise. This test appears to be important for further interpretation.

[27] The effect of the reference model change upon the results is investigated in a test shown in Figure 5. The first result (Figure 5, top) corresponds to the main model obtained based on the AK135 model. For another inversion (Figure 5, bottom) I used a model in which 3% higher velocity is defined the uppermost layer, and the difference between the models linearly decreases down to 700 km depth. It can be seen that the main configuration of anomalies remains unchanged despite considerably different velocity gradient in the reference model. In the passive tomography the origin times of sources are unknown, and we use the relative residuals. For regional and teleseismic rays, which are mostly used in this study, changing the reference model biases the absolute times, but the residuals usually change weakly. Change of absolute reference velocity also shifts the raypaths that should bias the retrieved anomalies up or down. However, in practice, these changes in the results are minor in respect to the vertical resolution uncertainty of the model.

[28] The resolution of the resulting model was checked based on synthetic simulations using different model configurations. These tests were also used to define the optimal inversion parameters in each of the 32 circular areas covering the study region. The results of synthetic modeling for a model with realistic configuration of anomalies and two checkerboards are presented below.

[29] A model with realistic anomalies was defined in the central part of the study area covering much larger space than a single inversion window (Figure 6, column 1). The anomalies were defined inside prisms with unchanged shapes in some depth intervals. The shapes of these synthetic anomalies were digitized based of results of real data inversion in four depth sections.

[30] The synthetic residuals were computed along the raypaths traced in the 1-D spherical model, implying a linear approach. As previously discussed, the performance of full 3-D ray tracing would require much longer computation time, which would limit the number of tests. The advantages of fast calculation performance fully compensate for the shortcomings related to neglecting the nonlinear effect. Relatively fast processing allowed for many trials aimed at finding the optimal values of free parameters to be run, which were then used for the inversion of the real data.

[31] Random noise with a statistical distribution having the same shape of the residuals distribution in the ISC catalog was added to the synthetic residuals. The amplitude of the noise was defined separately for the *P* and *S* data in order to obtain the same value of variance reduction after synthetic inversion as in the real data case. It should be noted that the noise level defined according to this criteria depends on the configuration of the anomalies. The defined noise level is weaker for the smaller synthetic anomalies. For the synthetic model with realistic anomalies, the noise

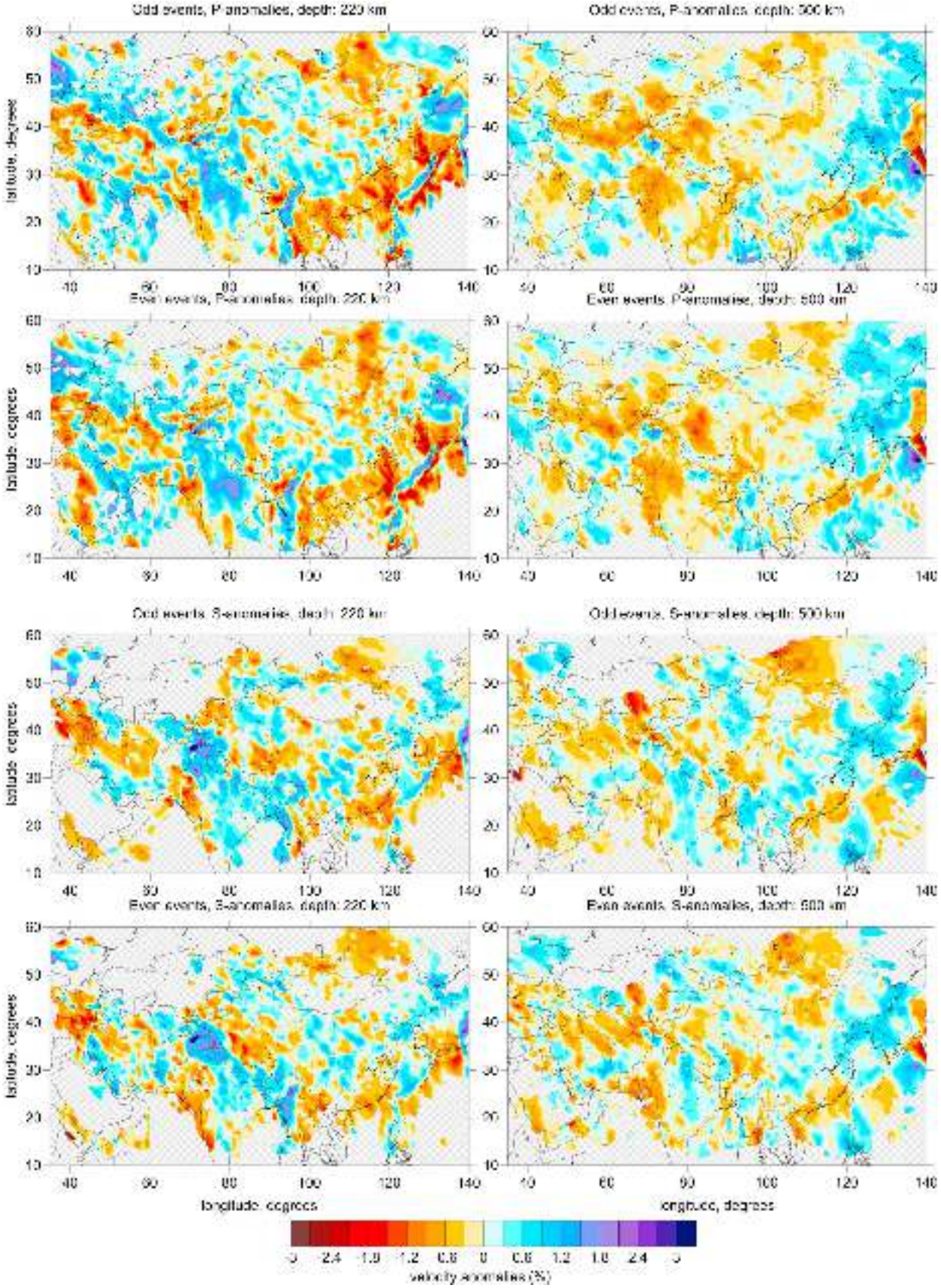

Figure 4. Odd-even test: the independent inversion of two data subsets (with odd and even numbers of events). Results for two depths (220 and 500 km) for *P* and *S* models are presented. Comparison of the results for the odd and even subsets reveals the effect of random noise.

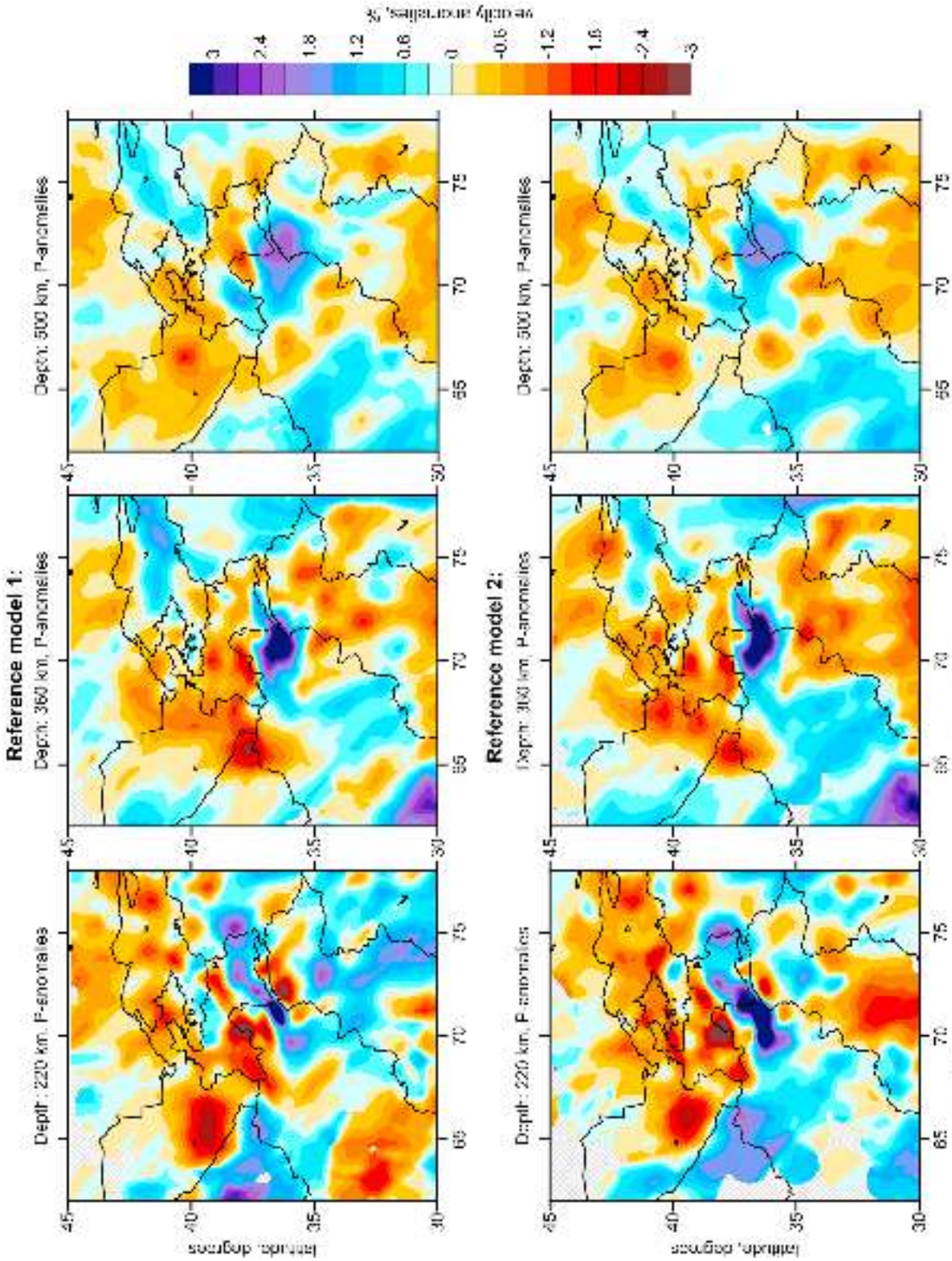

Figure 5. Reconstruction results based on two different reference models. (top) A fragment of the main *P* velocity model in three horizontal sections. (bottom) Result of processing of the same data, but with 3% higher reference *P* velocity values in the uppermost layer which linearly decreases down to 600 km depth.

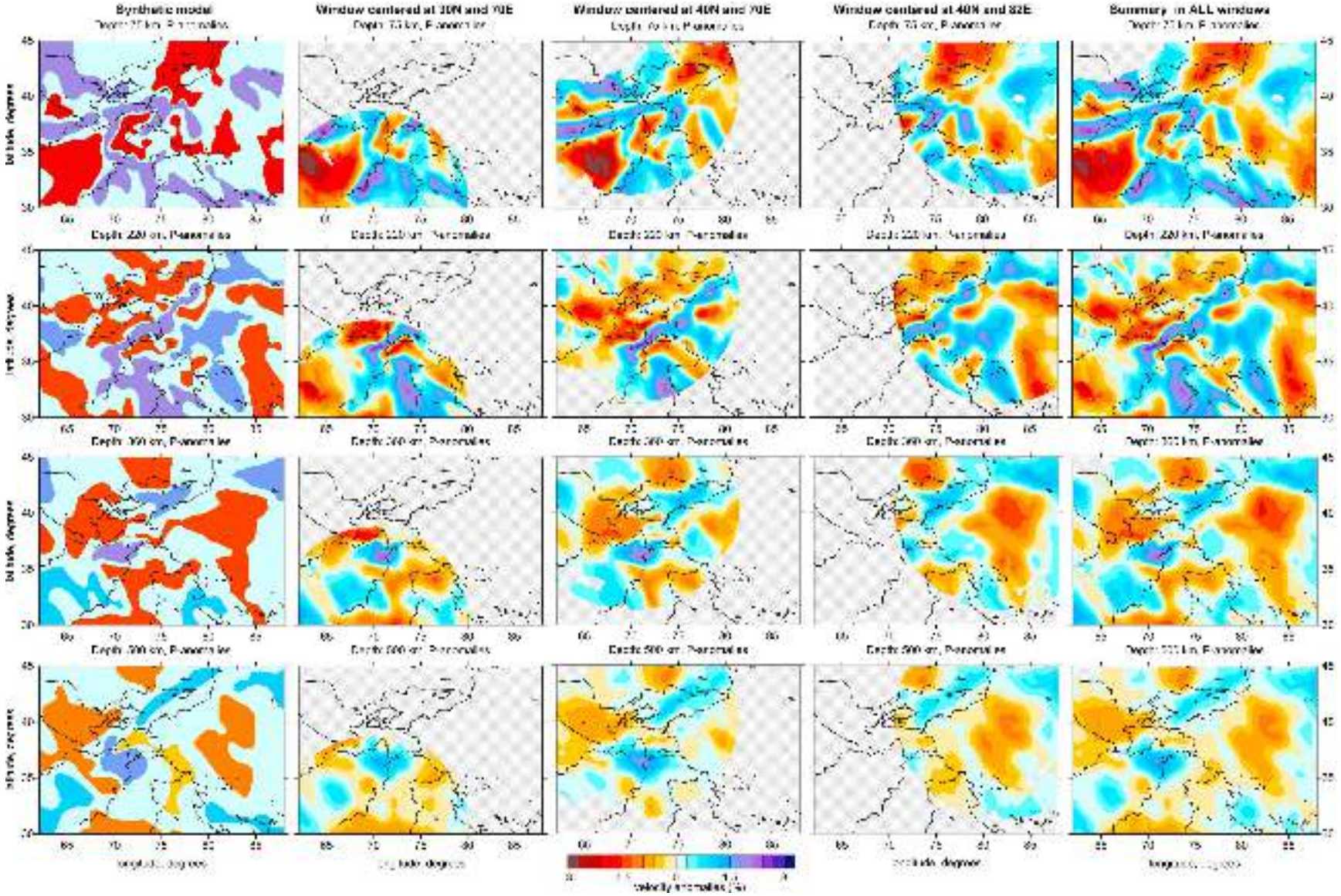

Figure 6. Result of reconstruction of the real-shaped synthetic model in a set of overlapping circular windows. Column 1 represents synthetic model at different depths. Columns 2 to 4 show examples of the inversion results in three separate windows. Average model of synthetic reconstruction is shown in column 5.

level for *P* and *S* models was equal to 0.4 and 0.8 s, respectively. Same level was defined for the checkerboard model with 3° × 4° and 5° × 6° size of *P* and *S* anomalies, respectively. For a model with smaller patterns (2° × 2° and 3° × 4°) the noise was smaller: 0.3 and 0.6, for *P* and *S* data, respectively.

[32] The reconstruction procedure for each circular area was the same as in the case of the real data inversion, including the step of the source location.

[33] The synthetic residuals were computed using the same source/receiver pairs as in the real data inversion. It is important that when computing synthetic residuals for rays traveling partly outside the inversion window, the outside anomalies affect the traveltimes. This causes the accumulation of additional residuals that can be considered as noise.

[34] Reconstruction results for the model with realistic synthetic anomalies are shown in Figure 6 for three selected windows and for the summary model. It can be seen that the outside anomalies do not have any significant effect upon the inversion results. In the summary model, all defined anomalies are reconstructed at correct positions. Fairly robust reconstruction of anomalies located inside a current window indicates that the algorithms are able to separate the partitions in the residuals related to the inside and outside anomalies. This can be explained by rather dense azimuthal coverage provided by the ISC data. Thus the residuals due to outside anomalies are considered as random noise which has no coherent signal with other data crossing the target area in other directions. As we see in the reconstruction results, the effect of the outside partitions of the residuals upon results in well illuminated areas is rather weak.

[35] To show the spatial resolution of the tomographic model, I also present the results of two checkerboard tests (Figure 7). The results are shown for the depths that correspond roughly to the middle points of three layers with different signs of checkerboard anomalies. The models correspond to two different runs of a simultaneous reconstruction of the *P* and *S* models. The first case reproduces the checkerboards with lateral sizes of 2° × 2° for the *P* model and 3° × 4° for the *S* model. The second run uses cell sizes of 3° × 4° for the *P* model and 5° × 6° for the *S* model. The images can be used to estimate the capacity of the algorithm in retrieving fixed size anomalies. When small-scale anomalies are reliably restored, the larger patterns will be restored with the same or better quality. In addition, the checkerboard tests allow the identification of areas of possible smearing due to uneven azimuthal distribution of the rays. Analysis of the results of the checkerboard tests in Figure 7 allows the estimation of the robustness of different size anomalies in the resulting model. For example, for the *P* model, anomalies of about 200 km size (Figure 7c) can be retrieved in limited parts of the study area where the maximum seismic activity is observed. At the same time, ~300 km size patterns (Figure 7a) are reconstructed in most parts of the study area. In central areas with the best resolution, both the shapes and amplitudes of the anomalies are correctly retrieved, while in marginal areas, the fit is observed on a qualitative level. These results reveal rather good vertical resolution of the model. The change in sign at 300 km and 600 km depth is robustly resolved in most parts of the study area. We see that in areas with moderate resolution we observe diagonal smearing along SE–NW direction which can be explained by dominant orientations or rays traveling to European stations. This effect should be taken into account when interpreting the real data inversion results.

[36] All the presented tests show that most patterns in the *P* and *S* models appear to be robust, and that they can be used for geodynamical interpretation.

4. Discussion of Results in Selected Regions

[37] Horizontal and vertical sections for selected parts of the derived model of *P* velocity anomalies are presented in sections 4.1–4.3. Only brief discussions of the main patterns beneath these areas are presented. More detailed descriptions and geodynamical interpretations of the tomographic model beneath the Iran, Pamir-Hindukush, and Burma regions will be given in separate papers, which are presently in preparation.

4.1. Iran and Surrounding Regions

[38] The first area of the tomographic model includes Iran and the surrounding regions. The Iran region consists of actively deformed orogenic belts located between two large rigid tectonic units: the Arabian plate in the south and the Turan segment of the Eurasian plate in the north (Figure 8). The collision with the Arabian plate in southern Iran is marked by the Zagros and Makran thrust belts. In the north, the Caucasus, Alborz, and Kopet Dagh thrust belts lie along the southern border of the Eurasian plate. The Iranian Plateau, which has a complex structure consisting of several microplates separated by folded belts, is located between these two thrust systems.

[39] The distribution of *P* velocity anomalies is shown in two horizontal and four vertical sections in Figure 9. The distributions of *S* velocity anomalies are very similar for this area. In general, the presented tomographic model in Iran fits with most previous studies based on surface waves [e.g., *Maggi and Priestley*, 2005; *Mokhtar et al.*, 2001; *Rodgers et al.*, 1999; *Mindevalli and Mitchell*, 1989] and body waves [e.g., *Hearn and Ni*, 1994; *Al-Lazki et al.*, 2003, 2004; *Alinaghi et al.*, 2007]. Note that the model by *Alinaghi et al.* [2007] was obtained based on the same tomographic approach as that used in this study, but with a much smaller data set.

[40] In most of these models, in the uppermost mantle the Iranian and Turkish plateaus are characterized by generally low velocities, while higher velocities are observed beneath the Zagros and Makran folded belts and beneath the Turan plate. In the lower part of the upper mantle (e.g., at 500 km depth), these features are reversed: higher velocities are present beneath central Iran and lower velocities are to the south and north. Based on these and other geophysical observations, most researchers agree that the Arabian plate is subducting beneath Iran [e.g., *Molinaro et al.*, 2005]. In the presented tomographic model, the high-velocity patterns in the vertical sections apparently look similar to the subduction model. However, there is no evidence of deep seismicity beneath Zagros [*Engdahl et al.*, 2006]. It probably means that the penetration of the transitional Arabian lithosphere to the mantle has a different mechanism than a classical oceanic subduction with the Benioff zone. A more detailed consideration of the tomographic results implies that this high-velocity anomaly, which is interpreted by some authors as

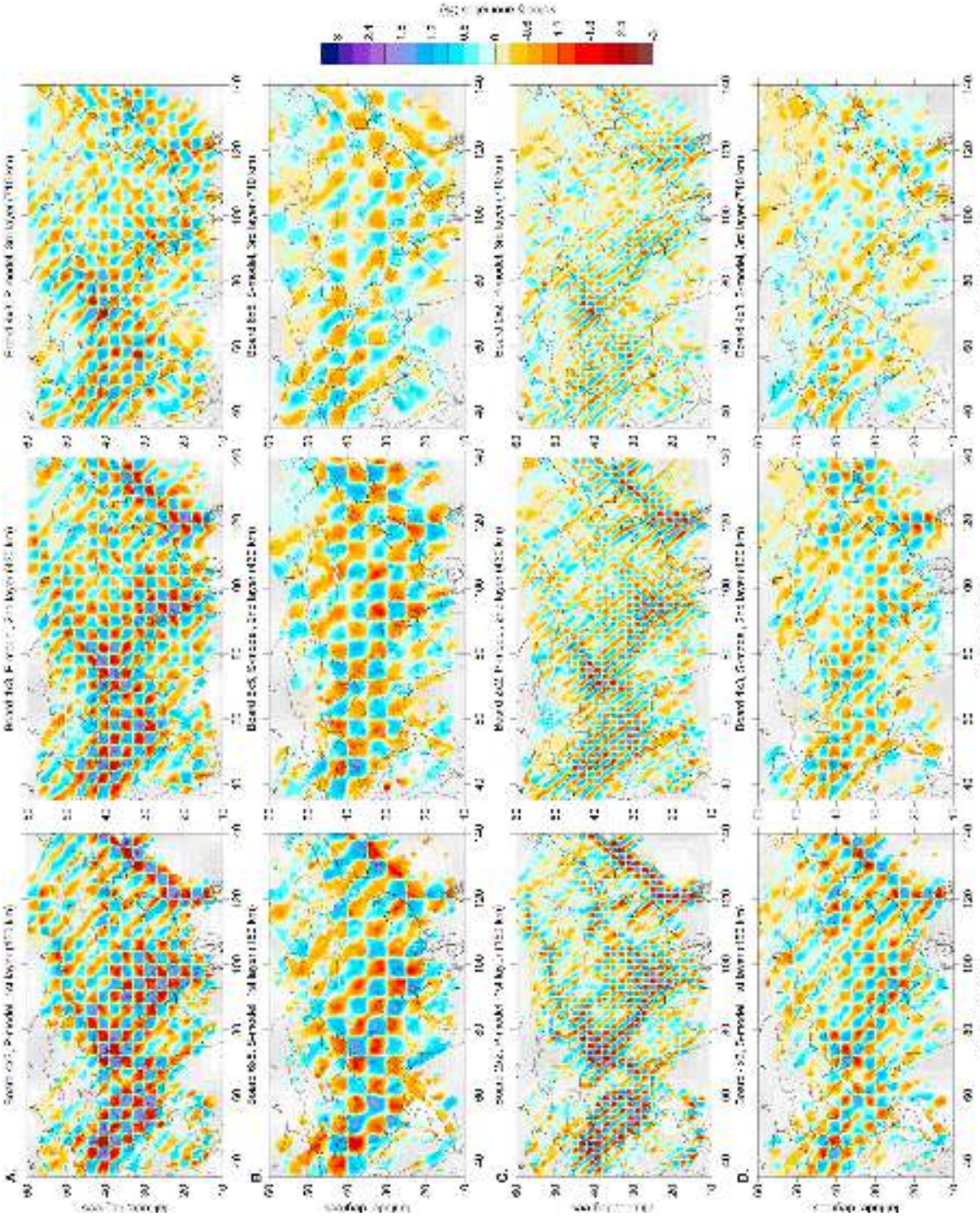

Figure 7. Two checkerboard tests. The size of the synthetic patterns are (a and b) $3° \times 4°$ and $5° \times 6°$ for the *P* and *S* models, respectively, and (c and d) $2° \times 2°$ and $3° \times 4°$ for *P* and *S* models, respectively. In both cases, the signs of the anomalies change at 300 and 600 km. The sections roughly represent the midpoint of the depth interval of each checkerboard layer.

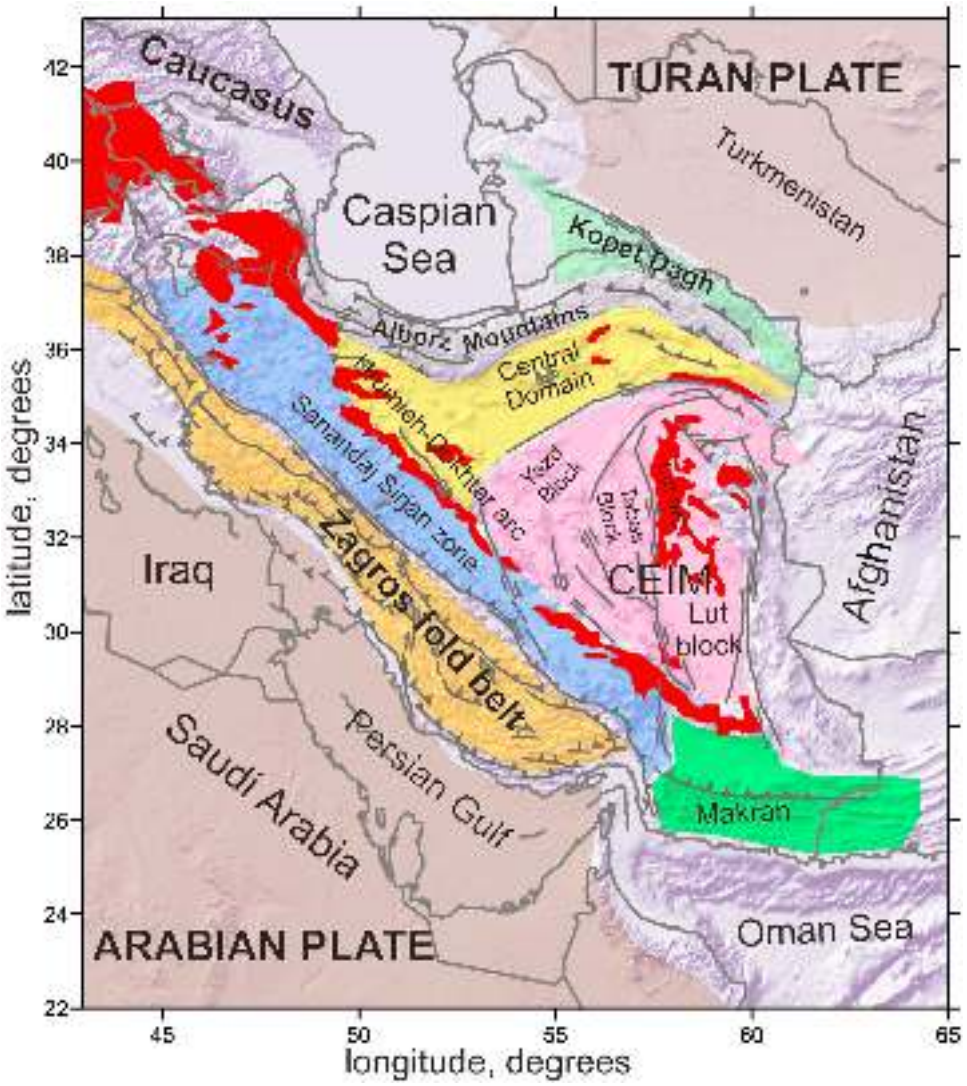

Figure 8. Main tectonic units in Iran compiled from *Nezafati* [2006], *Verdel et al.* [2007], *Stöcklin* [1968], and *Takin* [1972] overlaid on a shaded relief map. Zones of Cenozoic volcanism are marked with solid red. CEIM is the central east Iran microplate. The main tectonic units in Iran and surrounding regions are highlighted with different colors.

the subducting Arabian lithosphere, is not homogeneous. Several checkerboard tests performed in this study show that the resolution of the model in this area is sufficient to resolve patterns less than 200 km in size. The odd-even test provides consistent features that prove the robustness of the main patterns beneath Iran and the surrounding areas. Based on the derived *P* and *S* velocity models, the high-velocity pattern in S and SW Iran does not appear to be a continuous conveyer, as in a classic case of oceanic subduction. At shallow depths, the subduction zone appears to be separated into two parts corresponding to the Zagros (Z) and Makran plates (M). In deeper sections, the separation of the high-velocity anomaly into two bodies becomes clearer.

[41] The Zagros segment (Section 2A–2B in Figure 9) displays a steeply dipping high-velocity anomaly. The descent of the Makran plate (Section 3A–3B in Figure 9) seems to be more complicated. The subducting plate reaches a depth of ~400–500 km and then appears to be stacked there. Only a part of this high-velocity material penetrates to deeper sections. In map view at 500 km, a zone of accumulation of the Makran high-velocity material seems to be rather complex.

[42] The Makran plate in southeast Iran is presumably oceanic, and it subducts southward without pushing considerably into the continental crust of Iran. On the contrary, the Zagros segment in southwest Iran is represented by a transitional ocean-to-continent type lithosphere. When penetrating to the upper mantle, it strongly affects the overriding plate and causes large amounts of shortening of the overriding plate in western Iran. This transition from strong shortening in the west to weak in the east is observed in a number of right-lateral transform faults [e.g., *Takin*,

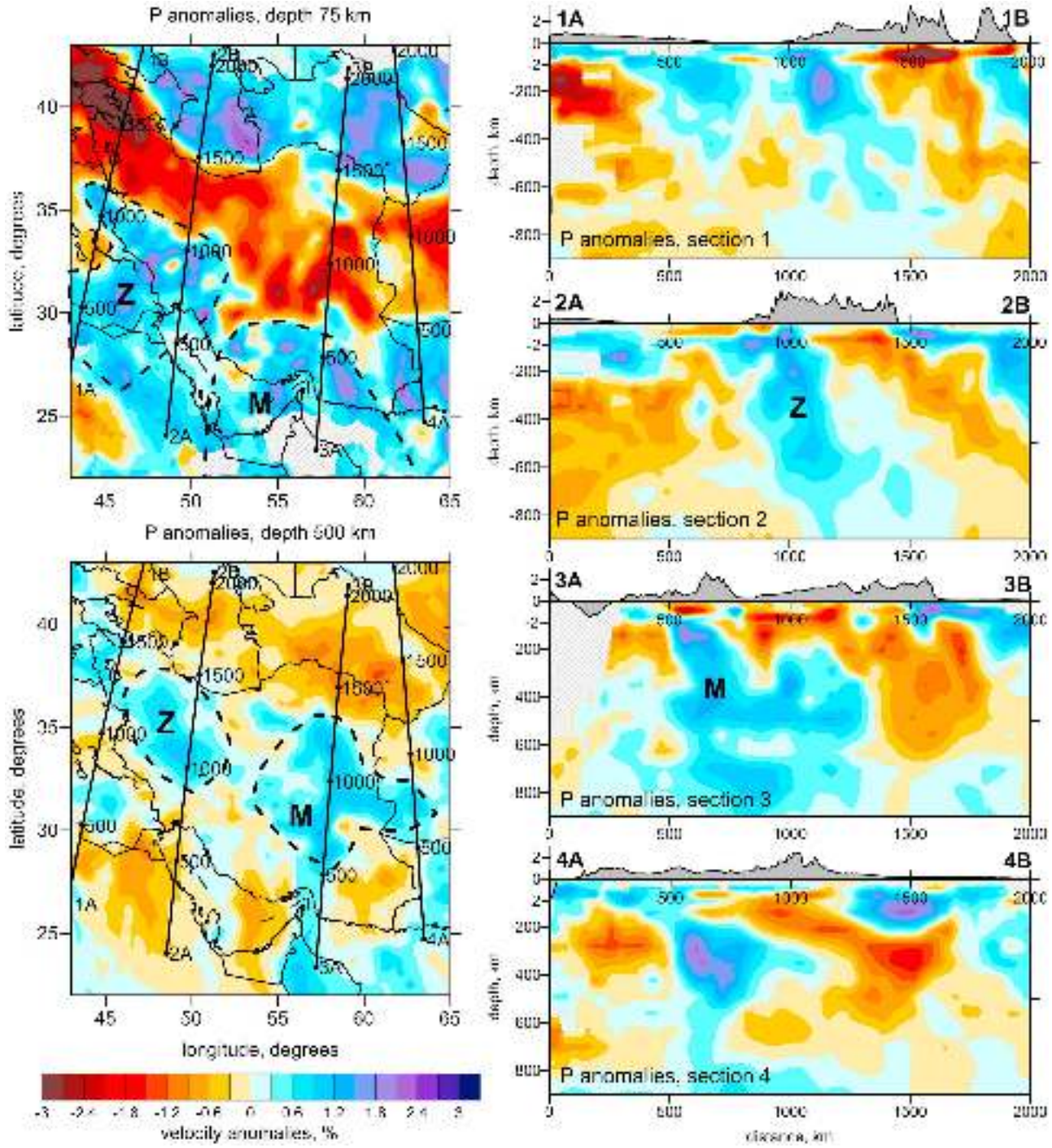

Figure 9. Two horizontal and four vertical sections of the resulting *P* velocity model for Iran. Relief in km is shown in gray colors above each section. Dotted lines highlight the locations of the Zagros (Z) and Makran (M) plates.

1972] and in GPS measurements [*Vernant et al.*, 2004; *Masson et al.*, 2007].

[43] In Iran, strong Cenozoic volcanic activity is reported along the Urumieh-Dokhtar zone (see Figure 8), which is oriented NW–SE along the Zagros fold belt [e.g., *Haghipour and Aghanabati*, 1985]. Another volcanic field is observed in central eastern Iran within the Lut block. The uppermost mantle beneath these volcanoes appears to be low velocity (see map at 75 km depth). However, they are located just above high-velocity anomalies in the tomographic models in deeper sections. For both the Zagros and Makran segments, the observed Cenozoic volcanism may be due to the subduction of the Arabian lithosphere beneath Iran [*Kazmin et al.*, 1986], similar to classical oceanic

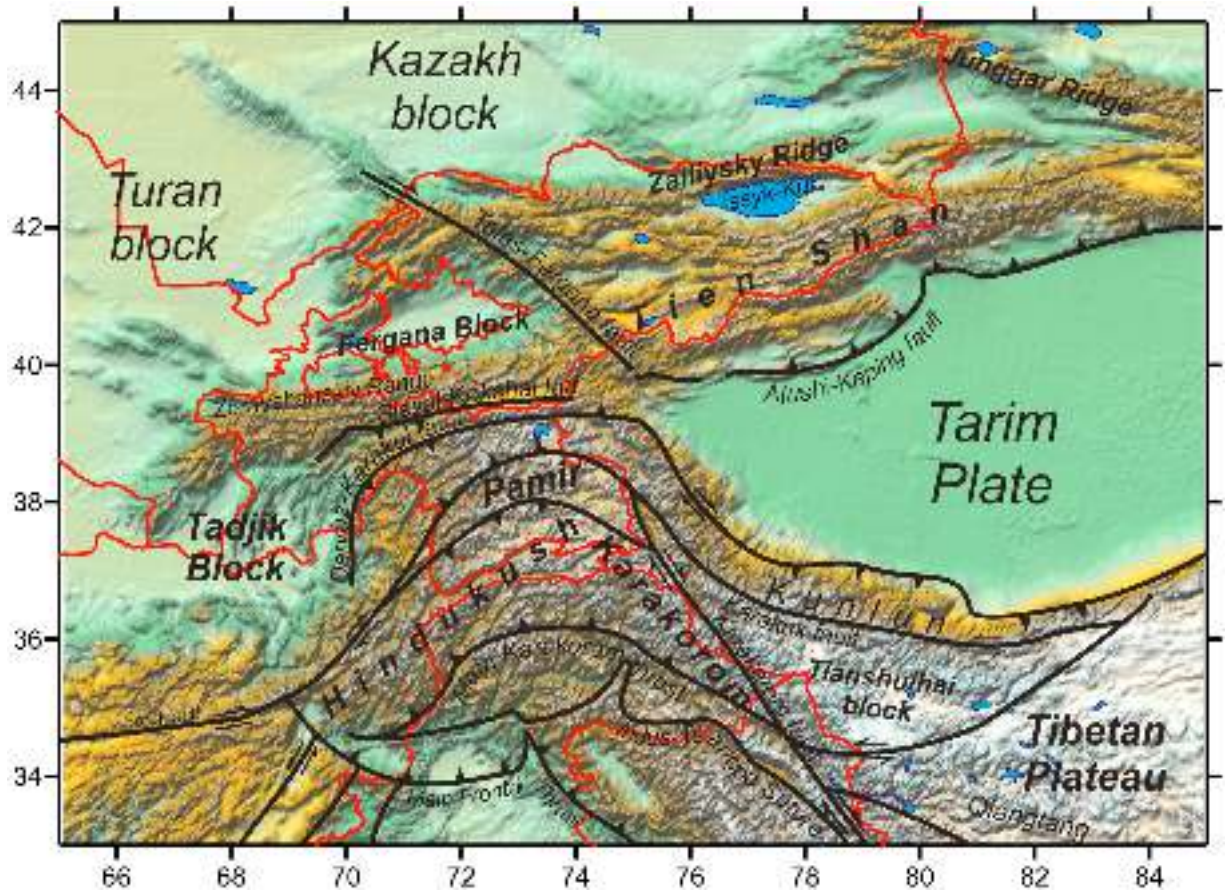

Figure 10. Main tectonic units in central Asia. Red lines indicate political boundaries.

subduction. Note that the gap between the Zagros and Makran blocks corresponds to a low density of volcanic features in the Urumieh-Dokhtar arc.

4.2. Pamir, Hindukush, and Tien Shan Regions

[44] This section presents the results for central Asia, which includes large mountain ranges of the Pamir, Hindukush, and Tien Shan (Figure 10). These orogenic belts are located between rigid lithospheric blocks: the Indian plate in the south, Tadjik Block in the west, the Turan plate and Fergana microplate in the northwest, the Kazakh block in the north, and the Tarim block in the east (Figure 10). The mountain building in the interblock areas is caused by the northward displacement of the Indian plate at a rate of about 4 cm yr^{-1} [*De Mets et al.*, 1994]. An important feature of the Pamir–Hindukush region is the fairly high concentration of intermediate-depth earthquakes, which reach depths of 300 km [e.g., *Chatelin et al.*, 1980; *Lister et al.*, 2008]. This is one of the most tectonically active areas in the world, where intermediate-depth seismicity occurs beneath the continent and is apparently not related to oceanic subduction.

[45] The deep structure beneath this area has been investigated in many studies. The first teleseismic tomography studies by *Lukk and Vinnik* [1975] and *Vinnik et al.* [1977] reported faster seismic velocities associated with the Pamir–Hindukush deep seismic zone. Similar features have been observed in global tomographic models [*Bijwaard et al.*, 1998; *van der Voo et al.*, 1999; *Replumaz et al.*, 2004, 2010]. According to these studies, a northward dipping high-velocity body is observed in the entire upper 600 km of the mantle and below the Hindukush region in northeastern Afghanistan and southern Tajikistan. The same feature was observed in our previous regional upper mantle tomographic model [*Koulakov and Sobolev*, 2006], which was derived based on a nearly identical algorithm as in this study, but using a smaller data set.

[46] Most authors agree that this high-velocity body coinciding with the distribution of deep earthquakes represents the subduction zone. However, questions about the direction of the subduction and how many slabs are present are still actively debated. Based on information on opposite dips of the seismicity in the Pamir and Hindukush segments, some authors have suggested that two distinct slabs, the Indian and Asian slabs, subduct in opposite directions [e.g., *Chatelin et al.*, 1980; *Roecker*, 1982; *Burtman and Molnar*, 1993; *Fan et al.*, 1994]. The alternative model attributes the observed seismicity and mantle seismic structure in the region to only the northward subduction of the Indian plate, which overturns beneath the Pamir [*Billington et al.*, 1977; *Vinnik et al.*, 1977; *Pegler and Das*, 1998; *van der Voo et al.*, 1999; *Pavlis and Das*, 2000; *Koulakov and Sobolev*, 2006]. In a later paper [*Koulakov et al.*, 2010], we proposed an alternative explanation of the occurrence of deep seismicity coinciding with high velocities in the

upper mantle beneath the continental areas of Vrancea (Romania) and Pamir-Hindukush based on the delamination mechanism.

[47] The resulting *P* velocity anomalies are presented in vertical and horizontal sections in Figure 11. In shallow sections (e.g., 75 km and 220 km depth), the anomalies in the Pamir-Hindukush area appear as alternating elongated belts oriented along the main sutures and thrusts (see Figure 10). Deeper sections display a prominent high-velocity anomaly beneath Hindukush that seems to be isometric in map view. The shape of this vertically oriented body can also be seen in two vertical sections, 1A–1B and 2A–2B. In the upper part at ~200 km depth, the body appears to be thinner than in deeper levels, and coincides with very intensive intermediate-depth seismicity. This high-velocity pattern is quite similar in shape to a flow of honey poured from a cap. In the upper part, nearly the cap border, such flow is flat as a wall, while in lower part it forms an isometric drop. The thin part of this body, with strong seismicity, looks like the necking zone of a nearly detached honey drop.

[48] These features appear to be representative of delamination, not subduction. First, this anomaly does not look like a flat "conveyer" as should be in a case of classical subduction. The width of the Hindukush anomaly is relatively small compared to the length. It is especially difficult to imagine the coexistence of two oppositely dipping slabs, as has been proposed by some authors, in this narrow zone. Second, it remains unclear where sinking dense oceanic lithosphere would have originated. The latest oceanic basin in this area closed several dozen million years ago [e.g., *de Sigoyer et al.*, 2000; *Clift et al.*, 2002]. In addition, subduction of continental lithosphere is not plausible; the negative buoyancy of continental lithosphere that would allow it to sink is under debate.

[49] Delamination, as opposed to subduction, was initially proposed as an alternative mechanism of lithospheric "recycling" in continental collision areas by *Bird* [1978] and further developed by other authors [e.g., *Kay and Kay*, 1993; *Sobolev et al.*, 2006; *Babeyko et al.*, 2006]. The delamination process is initiated by strong compression and shortening of continental areas. Such deformation leads to considerable thickening of the crust (both felsic and mafic layers) in areas with the weakest lithosphere. The mafic material in the lower crust is transformed to dense eclogite. When it achieves a critical mass, the eclogite starts to sink. This triggers the detachment of the mantle part of the lithosphere, which begins to descend as it is entrained by the eclogitic drop. According to estimates presented by *Babeyko et al.* [2006], the sinking of eclogite and entrained lithosphere is much faster than the rate of subduction and convection. Abrupt changes of *P-T* conditions inside this drop may cause high stresses and water release from entrained crustal material that create the conditions for active seismicity at great depths. After delamination, the crust above the descending drop consists mostly of a thick felsic part that can be associated with low seismic velocities, which was similar to those that are clearly seen in our tomographic results. Delamination leads to high topography [e.g., *Sobolev et al.*, 2006], which is present in this area.

[50] The image of the high-velocity anomaly beneath the Pamir-Hindukush region is somewhat similar to the results obtained for the Vrancea (Romania) [*Koulakov et al.*, 2010], where a similar delamination mechanism might take place on a smaller scale. There we observed a similar high-velocity body and intermediate depth seismicity in a very narrow, vertically oriented cluster. Delamination may be one of the main mechanisms of lithosphere recycling in areas of continent-continent collisions, and it may occur in any region of lithosphere shortening. However, the accumulation time of the unstable material is much longer than the time of the descent. Presently, these drops are observed in only two places in Eurasia: Vrancea and Pamir-Hindukush.

[51] In the Tien Shan, the tomographic model in this study is comparable to other results obtained on a regional scale. For example, results of receiver function tomography [*Vinnik et al.*, 2004] revealed generally similar features as in the model presented here. In particular, *P* velocity anomalies at 100 km depth in this model are quite similar to the *S* velocity distribution at 130 km depth in the results of *Vinnik et al.* [2004, Figure 14]. A similar shape of the inclined high-velocity anomaly is observed beneath the Tien Shan in the results of teleseismic tomography by *Makarov et al.* [2010] and *Zhiwei et al.* [2009].

[52] The structure beneath the Tien Shan can be observed in the vertical Section 4A–4B in Figure 11. The prominent high-velocity anomaly beneath Tarim down to a depth of 250 km probably represents the cratonic-type lithosphere. Beneath the Tien Shan, we observe a northward dipping high-velocity anomaly that penetrates to the upper mantle down to the transition zone at 670 km. This inclined anomaly seems to be separated from the Tarim lithosphere. In map view at 360 km and 500 km, this anomaly seems to be elongated in the SW–NE direction, parallel to the NW border of Tarim. This inclined body may represent the detached mantle portion of the continental lithosphere of Tarim. At the same time, we do not observe a trace of southward dipping Kazakh block as reported by *Zhiwei et al.* [2009]. Detailed interpretation of the lithosphere behavior beneath Tien Shan will be given in a separate paper based on the joint analysis of numerical modeling and tomographic results.

4.3. Burma

[53] Shapes of the main tectonic blocks in the Burma region and a schematic reconstruction of their locations for the time of about 10 Ma ago are presented in Figure 12. It can be seen that Burma plate is located between the obliquely moving Indian plate and the Indochina block. Figure 13 presents the portion of the *P* velocity model for the Burma region and the northern part of the Andaman Arc. Similar to most previous tomographic studies [e.g., *Replumaz et al.*, 2010; *Li et al.*, 2008; *Bijwaard et al.*, 1998; *Huang and Zhao*, 2006], the classical shape of subduction beneath Burma is apparent. A linear high-velocity anomaly between 21°N and 27°N latitude coincides with the distribution of intermediate depth seismicity that occurs down to ~200 km depth. As shown in vertical Sections 1A–1B and 2A–2B, this anomaly steeply dips eastward and reaches depths of 500 to 600 km. This is deeper than reported by *Li et al.* [2008] and *Replumaz et al.* [2010], who observed this anomaly down to 300 and 400 km depth, respectively. Also, unlike the model presented by *Replumaz et al.* [2010], these results show that, in shallow sections (e.g., 220 km depth), the Burma high-

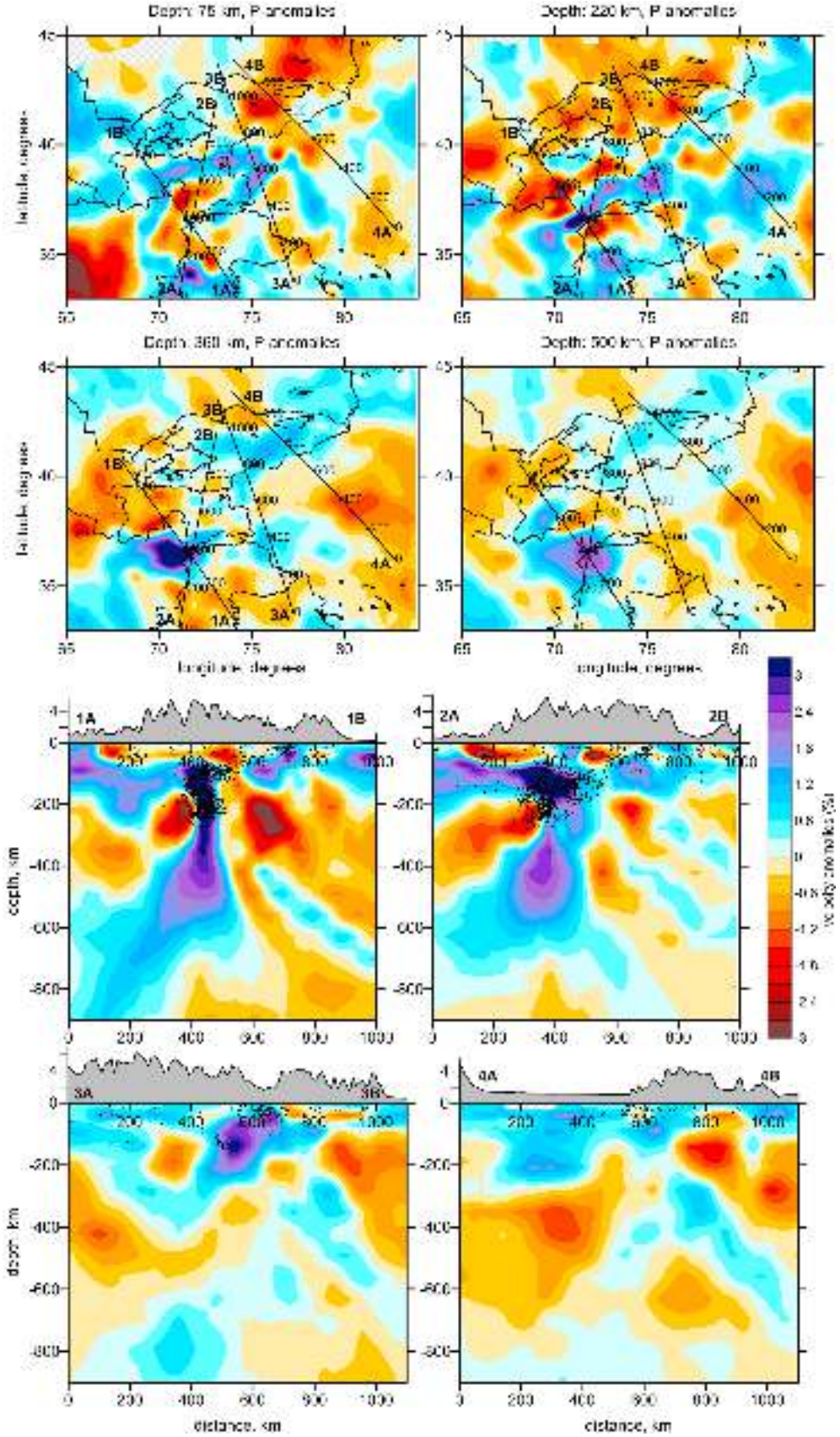

Figure 11. Four horizontal and four vertical sections of the resulting *P* velocity model for central Asia (Pamir, Hindukush, Tien Shan, and Tarim). Black points in vertical sections mark the locations of events at distances of <80 km from the profile. Relief in km is shown by gray color above each section.

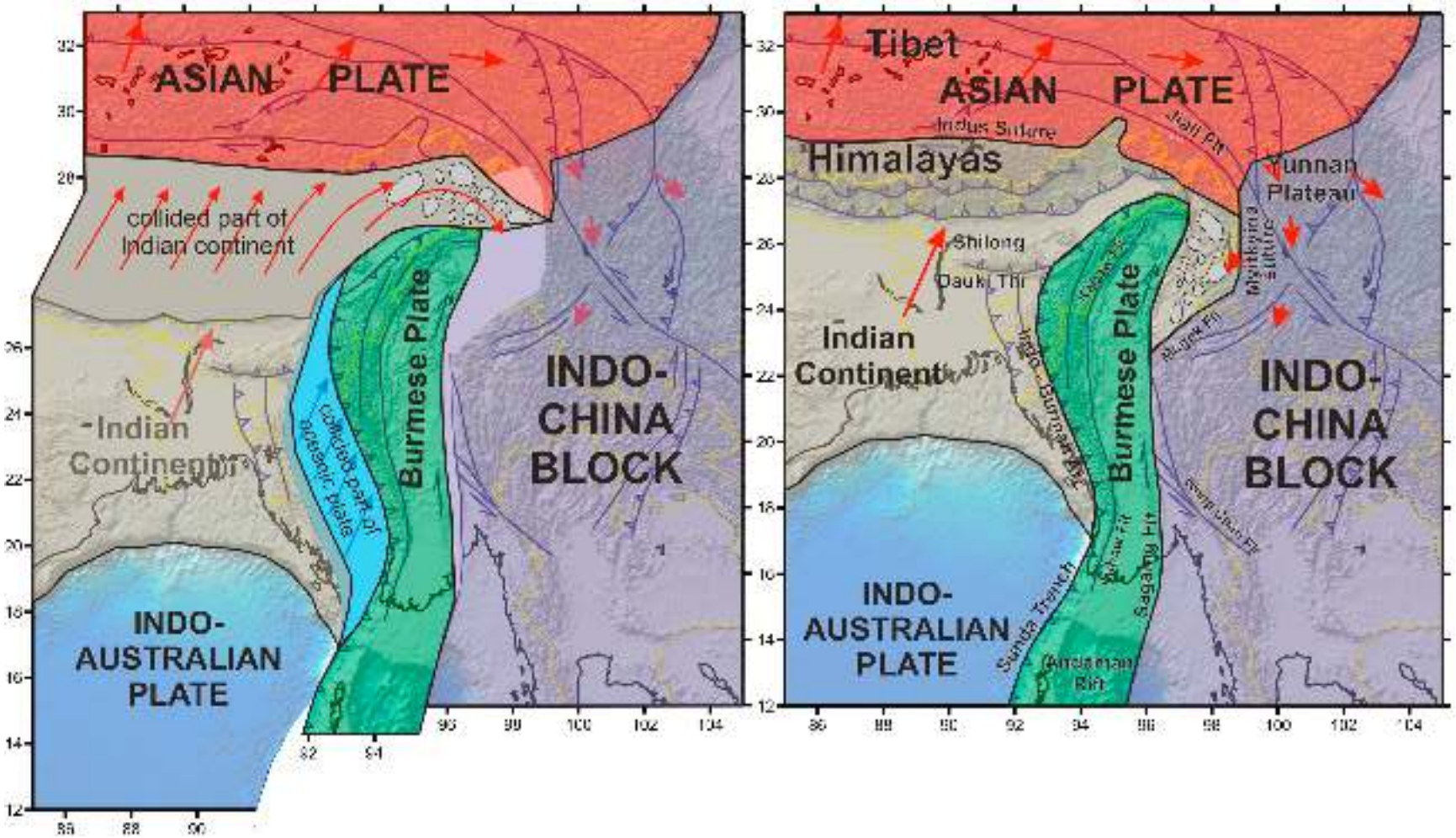

Figure 12. (left) Reconstruction of the main block configuration about 10 Ma ago. (right) Main tectonic units around Burma in present time.

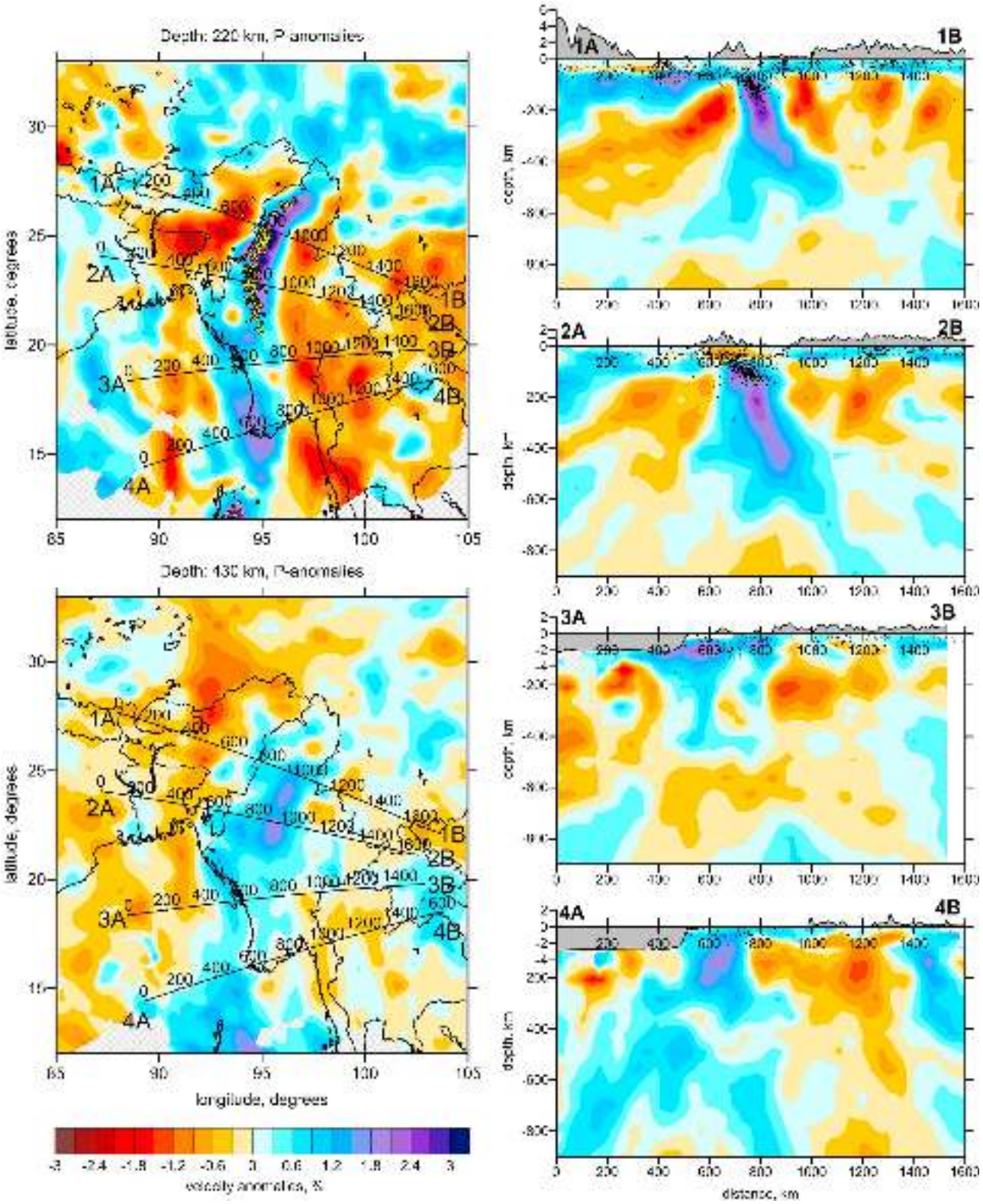

Figure 13. Two horizontal and four vertical sections of the resulting *P* velocity model for Burma and surrounding areas. Yellow dots in map at 220 km depth indicate seismic events deeper than 100 km. Black points in vertical sections mark the locations of events at distances of < 80 km from the profile. Relief and Sea bathymetry in km is shown by gray color above each section.

velocity anomaly appears to be connected with the Andaman subduction zone. At the same time, the behavior of anomalies south to Burma is quite complex. In Section 3A–3B, the high-velocity anomaly is still present down to 400 km depth, but seems to be almost vertical and less prominent. Further to the south (Section 4A–4B), the large high-velocity anomaly appears again, but it seems to be oriented westward. In this section, no Benioff seismicity is observed. The eastward dipping Benioff seismicity appears further to the south in the Sunda arc, which is outside of the presented model. In deeper sections (430 km), the anomalies beneath Burma and Andaman seem to be separated.

[54] Subduction in Burma remains a rather enigmatic phenomenon with an unclear mechanism. Indeed, available GPS observations [e.g., *Sahu et al.*, 2006] show that the relative plate motion of about 36 mm yr^{-1} between India and Indochina mostly occurs in the regional Sagaing strike-slip fault (Figure 12). Almost no eastward shortening of India toward Indochina occurs along the Indo-Burmese arc. Thus the presence of high-velocity material beneath Burma, which probably represents the subducting lithosphere, cannot be explained by the present-day plate kinematics. This subduction can be partially explained by the S-shaped loop of the Indo-Burman arc (Figure 12). The NW–SE oriented segment of this loop between 18°N and 22°N enables sufficient shortening for the subduction due to the northward movement of the Indian plate. The problem with this scenario is that this loop is located rather far from the current location of the Burman slab. Another explanation could be the gradual rotation of the Indo-Burman arc together with the subduction zone, as proposed, for example, by *Replumaz et al.* [2010]. According to this scenario, the subduction occurred in previous stages when the orientation of the Burman arc allowed shortening due to the northward movement of the Indian plate. Now the orientation of the arc is parallel to the displacement vector and the subduction should be not active anymore. At the same time, different analyses of focal mechanisms have provided controversial conclusions on the slab behavior. In particular, *Rao and Kumar* [1999] argued that only strike-slip motion, and not dip-slip movements, are observed in the Burma Benioff zone. On the other hand, *Ni et al.* [1989] and *Dasgupta et al.* [2003] provided rather clear evidence for downdip extension within the subducted slab. In the latter case, sinking of the Burman slab would be possible if it is detached from the Indian lithosphere, because almost no movement of the Indian plate in the direction across the Burman subduction zone is observed. However, neither this model nor the results of previous tomographic studies provide any evidence for such detachment.

5. Conclusions

[55] This study presents a new model of high-frequency *P* and *S* velocity anomalies beneath Asia. Separate inversions were performed in overlapping windows that covered the study area. By individually tuning the inversion parameters in each window, we achieved the optimal conditions for the inversion in areas with different ray coverages. This enabled the resolution of higher-frequency patterns than in global inversions. This approach is not sensitive to large anomalies with sizes comparable with the diameter of the window. Thus, this approach is similar to high-frequency filtration of the velocity distribution. The reliability of the results is supported by resolving well-known structures in subduction zones and comparisons with existing tomographic models. The resolution and the effect of random noise were estimated using synthetic modeling and the odd/even test.

[56] The derived tomographic model provides important information about the lithospheric behavior beneath the Alpine-Himalayan collision belt. Several scenarios of lithospheric recycling were singled out based on the presented tomography results. Beneath Iran, we observed the subduction of two separate plates. The first, the Zagros plate, is probably transitional from an oceanic to a continental-type lithosphere and causes considerable shortening in western Iran. The second, the Makran plate, subducts as an oceanic plate without producing any apparent deformation of the overriding plate in Eastern Iran.

[57] Beneath Pamir and Hindukush, we observed a prominent high-velocity anomaly that looks more like a falling drop than a subducted slab. This may represent delamination of unstable mantle lithosphere triggered by the descent of dense eclogitic material that accumulated in the thickened lower crust. A similar process of delamination has been observed in the Vrancea region (Romania). I propose that delamination, not subduction, is the major mechanism of lithospheric recycling in areas of continent-to-continent collision. However, the time period of drop accumulation is much longer than the time of descent. Therefore, this process is observed in only two places in Eurasia, in Pamir and in Vrancea.

[58] The presented tomographic results show that the almost classical configuration of subduction in Burma with the presence of the Benioff seismicity zone and the conveyer-type high-velocity lithosphere sinking into the upper mantle. At the same time, the mechanism of Burman subduction remains enigmatic. According to available information about present-day plate kinematics, there is no shortening across this subduction zone, and it is unclear where the subducting material comes from. Further investigations based on 3-D numerical modeling and different geophysical observations are required to clarify this issue.

[59] **Acknowledgments.** I am grateful to the Chief Editor, Associate Editor, and both anonymous reviewers who provided thorough and friendly critical analysis of my work which helped to improve the manuscript. This work is supported by Heimholtz Society and RFBR joint research project 09-05-91321-SIG_a, multidisciplinary projects SB RAS 44, 21, and project ONZ RAS 7.4.

References

Al-Lazki, A. I., D. Seber, E. Sandvol, N. Turkelli, R. Mohamad, and M. Barazangi (2003), Tomographic Pn velocity and anisotropy structure beneath the Anatolian plateau (eastern Turkey) and the surrounding regions, *Geophys. Res. Lett.*, *30*(24), 8043, doi:10.1029/2003GL017391.

Al-Lazki, A. I., E. Sandvol, D. Seber, M. Barazangi, N. Turkelli, and R. Mohamad (2004), Pn tomographic imaging of mantle lid velocity and anisotropy at the junction of the Arabian, Eurasian and African plates, *Geophys. J. Int.*, *158*, 1024–1040, doi:10.1111/j.1365-246X.2004.02355.x.

Alinaghi, A., I. Koulakov, and H. Thybo (2007), Seismic tomographic imaging of *P*- and *S*-waves velocity perturbations in the upper mantle beneath Iran, *Geophys. J. Int.*, *169*(3), 1089–1102, doi:10.1111/j.1365-246X.2007.03317.x.

Babeyko, A. Y., S. V. Sobolev, T. Vietor, R. B. Trumbull, and O. Oncken (2006), Weakening of the upper plate during tectonic shortening: Thermo-mechanical causes and consequences, in *The Andes: Active Subduction Orogeny*, *Frontiers in Earth Sciences*, vol. 1, edited by O. Oncken et al., pp. 495–512, Springer, New York.

Bassin, C., G. Laske, and G. Masters (2000), The current limits of resolution for surface wave tomography in North America, *EOS Trans. AGU*, *81*, Abstract F897.

Bijwaard, H., W. Spakman, and E. R. Engdahl (1998), Closing the gap between regional and global travel time tomography, *J. Geophys. Res.*, *103*, 30,055–30,078, doi:10.1029/98JB02467.

Billington, S., B. I. Isacks, and M. Barazangi (1977), Spacial and focal mechanisms of mantle earthquakes in the Hindu Kush–Pamir region: A contorted Benioff zone, *Geology*, *5*, 699–704.

Bird, P. (1978), Finite element modeling of lithosphere deformation: The Zagros collision orogeny, *Tectonophysics*, *50*, 307–336, doi:10.1016/0040-1951(78)90140-3.

Boyd, F. R. (1989), Compositional distinction between oceanic and cratonic lithosphere, *Earth Planet. Sci. Lett.*, *96*, 15–26, doi:10.1016/0012-821X(89)90120-9.

Burtman, V. S., and P. Molnar (1993), Geological and geophysical evidence for deep subduction of continental crust beneath the Pamir, *Geol. Soc. Am. Spec. Pap.*, *281*, 76 pp.

Chatelin, J. L., S. W. Roecker, D. Hatzfeld, and P. Molnar (1980), Microearthquake seismicity and fault plane solutions in the Hindu Kush region and their tectonic implications, *J. Geophys. Res.*, *85*, 1365–1387.

Clift, P. D., A. Carter, M. Krol, and E. Kirby (2002), Constraints on India-Eurasia collision in the Arabian Sea region taken from the Indus Group, Ladakh Himalaya, India, *Geol. Soc. London Spec. Publ.*, *195*, 97–116.

Curtis, A., J. Trampert, R. Snieder, and B. Dost (1998), Eurasian fundamental mode surface wave phase velocities and their relationship with tectonic structures, *J. Geophys. Res.*, *103*, 26,919–26,947, doi:10.1029/98JB00903.

Dasgupta, S., M. Mukhopadhyay, A. Bhattacharya, and T. K. Jana (2003), The geometry of the Burmese-Andaman subducting lithosphere, *J. Seismol.*, *7*, 155–174, doi:10.1023/A:1023520105384.

De Mets, C., R. G. Gordon, D. F. Argus, and S. Stein (1994), Effects of recent revision to the geomagnetic reversal time scale on estimates of current plate motions, *Geophys. Res. Lett.*, *21*, 2191–2194.

de Sigoyer, J., V. Chavagnac, J. Blichert-Tift, I. Villa, B. Luais, S. Guillot, M. Cosca, and G. Mascle (2000), Dating the Indian continental subduction and collisional thickening in the northwest Himalaya: Multichronology of the Tso Morari eclogites, *Geology*, *28*, 487–490, doi:10.1130/0091-7613(2000)28<487:DTICSA>2.0.CO;2.

Ekström, G., J. Tromp, and E. Larson (1997), Measurements and global models of surface wave propagation, *J. Geophys. Res.*, *102*, 8137–8157, doi:10.1029/96JB03729.

Engdahl, E. R., R. D. van der Hillst, and R. P. Buland (1998), Global teleseismic earthquake relocation with improved travel times and procedures for depth determination, *Bull. Seismol. Soc. Am.*, *88*, 722–743.

Engdahl, E. R., J. A. Jackson, S. C. Myers, E. A. Bergman, and K. F. Priestley (2006), Relocation and assessment of seismicity in the Iran region, *Geophys. J. Int.*, *167*(2), 761–778.

Fan, G., J. F. Ni, and T. C. Wallace (1994), Active tectonics of the Pamirs and Karakorum, *J. Geophys. Res.*, *99*, 7131–7160.

Friederich, W. (2003), The *S*-velocity structure of the East Asian mantle from inversion of shear and surface waveforms, *Geophys. J. Int.*, *153*, 88–102, doi:10.1046/j.1365-246X.2003.01869.x.

Fukao, Y., A. To, and M. Obayashi (2003), Whole mantle *P* wave tomography using *P* and PP-P data, *J. Geophys. Res.*, *108*(B1), 2021, doi:10.1029/2001JB000989.

Griot, D., J. Montagner, and P. Tapponnier (1998), Phase velocity structure from Rayleigh and Love waves in Tibet and its neighboring regions, *J. Geophys. Res.*, *103*, 21,215–21,232, doi:10.1029/98JB00953.

Haghipour, A., and A. Aghanabati (1985), *Geological Map of Iran*, Min. of Mines and Metals, Geol. Survey of Iran, Tehran.

Hearn, T. M., and J. Ni (1994), Pn velocities beneath continental collision zones: The Turkish-Iranian plateau, *Geophys. J. Int.*, *117*, 273–283, doi:10.1111/j.1365-246X.1994.tb03931.x.

Huang, J. L., and D. P. Zhao (2006), High-resolution mantle tomography of China and surrounding regions, *J. Geophys. Res.*, *111*, B09305, doi:10.1029/2005JB004066.

International Seismological Centre (2001), Bulletin Disks 1–9 [CD-ROM], Int. Seismol. Cent., Thatcham, U. K.

Jordan, T. H. (1978), Composition and development of continental tectosphere, *Nature*, *274*, 544–548, doi:10.1038/274544a0.

Kay, R. W., and S. M. Kay (1993), Delamination and delamination magmatism, *Tectonophysics*, *219*, 177–189.

Kazmin, V. G., I. M. Sbortshikov, L.-E. Ricou, L. P. Zonenshain, J. Boulin, and A. L. Knipper (1986), Volcanic belts as markers of the Mesozoic-Cenozoic active margin of Eurasia, *Tectonophysics*, *123*, 123–152, doi:10.1016/0040-1951(86)90195-2.

Kennett, B. L. N., E. R. Engdahl, and B. Buland (1995), Constraints on seismic velocities in the Earth from traveltimes, *Geophys. J. Int.*, *122*, 108–124, doi:10.1111/j.1365-246X.1995.tb03540.x.

Koulakov, I. (1998), Three-dimensional seismic structure of the upper mantle beneath the central part of the Eurasian continent, *Geophys. J. Int.*, *133*, 467–489.

Koulakov, I. (2008), Upper mantle structure beneath southern Siberia and Mongolia from regional tomography data, *Russ. Geol. Geophys.*, *49*(3), 244–257.

Koulakov, I. (2009a), Out-of-network events can be of great importance for improving results of local earthquake tomography, *Bull. Seismol. Soc. Am.*, *99*(4), 2556–2563, doi:10.1785/0120080365.

Koulakov, I. (2009b), LOTOS code for local earthquake tomographic inversion. Benchmarks for testing tomographic algorithms, *Bull. Seismol. Soc. Am.*, *99*(1), 194–214, doi:10.1785/0120080013.

Koulakov, I., and N. Bushenkova (2010), Upper mantle structure beneath the Siberian craton and surrounding areas based on regional tomographic inversion of *P* and PP travel times, *Tectonophysics*, *486*, 81–100, doi:10.1016/j.tecto.2010.02.011.

Koulakov, I., and S. V. Sobolev (2006), A tomographic image of Indian lithosphere break-off beneath the Pamir-Hindukush region, *Geophys. J. Int.*, *164*, 425–440, doi:10.1111/j.1365-246X.2005.02841.x.

Koulakov, I., S. Tychkov, N. Bushenkova, and A. Vasilevskiy (2002), Structure and dynamics of the upper mantle beneath the Alpine-Himalayan orogenic belt from teleseismic tomography, *Tectonophysics*, *358*, 77–96, doi:10.1016/S0040-1951(02)00418-3.

Koulakov, I., et al. (2007), *P* and *S* velocity structure of the crust and the upper mantle beneath central Java from local tomography inversion, *J. Geophys. Res.*, *112*, B08310, doi:10.1029/2006JB004712.

Koulakov, I., M. K. Kaban, M. Tesauro, and S. Cloetingh (2009), *P* and *S* velocity anomalies in the upper mantle beneath Europe from tomographic inversion of ISC data, *Geophys. J. Int.*, *179*(1), 345–366, doi:10.1111/j.1365-246X.2009.04279.x.

Koulakov, I., B. Zaharia, B. Enescu, M. Radulian, M. Popa, S. Parolai, and J. Zschau (2010), Delamination or slab detachment beneath Vrancea? New arguments from local earthquake tomography, *Geochem. Geophys. Geosyst.*, *10*, Q03002, doi:10.1029/2009GC002811.

Kustowski, B., G. Ekström, and A. M. Dziewonski (2008), The shear-wave velocity structure in the upper mantle beneath Eurasia, *Geophys. J. Int.*, *174*, 978–992, doi:10.1111/j.1365-246X.2008.03865.x.

Li, C., R. D. van der Hilst, E. R. Engdahl, and S. Burdick (2008), A new global model for *P* wave speed variations in Earth's mantle, *Geochem. Geophys. Geosyst.*, *9*, Q05018, doi:10.1029/2007GC001806.

Lister, G., B. Kennett, S. Richards, and M. Forster (2008), Boudinage of a stretching slablet implicated in earthquakes beneath the Hindu Kush, *Nat. Geosci.*, *1*, 196–201, doi:10.1038/ngeo132.

Lukk, A. A., and L. P. Vinnik (1975), Tectonic interpretation of the deep structure of the Pamirs, *Geotect. Engl. Transl.*, *5*, 300-3004.

Maggi, A., and K. Priestley (2005), Surface waveform tomography of the Turkish-Iranian plateau, *Geophys. J. Int.*, *160*, 1068–1080, doi:10.1111/j.1365-246X.2005.02505.x.

Makarov, V. I., et al. (2010), Underthrusting of Tarim beneath the Tien Shan and deep structure of their junction zone: Main results of seismic experiment along MANAS profile Kashgar–Song-Kol, *Geotect. Engl. Transl.*, *44*(2), 102–126, doi:10.1134/S0016852110020020.

Masson, F., M. Anvari, Y. Djamour, A. Walpersdorf, F. Tavakoli, M. Daignières, H. Nankali, and S. van Gorp (2007), Large-scale velocity field and strain tensor in Iran inferred from GPS measurements: New insight for the Present-day deformation pattern within NE Iran, *Geophys. J. Int.*, *170*, 436–440, doi:10.1111/j.1365-246X.2007.03477.x.

Mindevalli, O. Y., and B. J. Mitchell (1989), Crustal structure and possible anisotropy in Turkey from seismic surface wave dispersion, *Geophys. J. R. Astron. Soc.*, *98*, 93–106.

Mokhtar, T. H., C. A. Ammon, R. B. Herrmann, and A. A. Ghalib (2001), Surface wave velocity across Arabia, *Pure Appl. Geophys.*, *158*, 1425–1444, doi:10.1007/PL00001228.

Molinaro, M., H. Zeyen, and X. Laurencin (2005), Lithospheric structure beneath the south-eastern Zagros Mountains, Iran: Recent slab break-off, *Terra Nova*, *17*, 1–6, doi:10.1l1/j.1365–3121.2004.00575.

Molnar, P., and P. Tapponnier (1975), Cenozoic tectonics of Asia: Effects of a continental collision, *Science*, *189*, 419–426, doi:10.1126/science.189.4201.419.

Nezafati, N. (2006), Au-Sn-W-Cu-mineralization in the Astaneh-Sarband area, west central Iran, including a comparison of the ores with ancient bronze artifacts from western Asia, Ph.D. thesis, Univ. of Tübingen,

Tübingen, Germany. (Available at http://tobias-lib.ub.uni-tuebingen.de/volltexte/2006/2533/)

Ni, J. F., M. Guzman-Speziale, M. Bevis, W. E. Holt, T. C. Wallace, and W. Seager (1989), Accretionary tectonics of Burma and the three-dimensional geometry of the Burma subduction zone, *Geology*, *17*, 68–71, doi:10.1130/0091-7613(1989)017<0068:ATOBAT>2.3.CO;2.

Paige, C. C., and M. A. Saunders (1982), LSQR: An algorithm for sparse linear equations and sparse least squares, *ACM Trans. Math. Soft.*, *8*, 43–47.

Pavlis, G. L., and S. Das (2000), The Pamir-Hindu Kush seismic zone as a strain marker for flow in the upper mantle, *Tectonics*, *19*, 103–115.

Pegler, G., and S. Das (1998), An enhanced image of the Pamir-Hindu Kush seismic zone from relocated earthquake hypocenters, *Geophys. J. Int.*, *134*, 573–595.

Piromallo, C., and A. Morelli (2003), *P* wave tomography of the mantle under the Alpine-Mediterranean area, *J. Geophys. Res.*, *108*(B2), 2065, doi:10.1029/2002JB001757.

Priestley, K., E. Debayle, D. McKenzie, and S. Pilidou (2006), Upper mantle structure of eastern Asia from multimode surface waveform tomography, *J. Geophys. Res.*, *111*, B10304, doi:10.1029/2005JB004082.

Rao, N., and M. Kumar (1999), Evidences for cessation of Indian plate subduction in the Burmese arc region, *Geophys. Res. Lett.*, *26*, 3149–3152.

Replumaz, A., H. Karason, R. D. van der Hilst, J. Besse, and P. Tapponnier (2004), 4-D evolution of SE Asia's mantle from geological reconstructions and seismic tomography, *Earth Planet. Sci. Lett.*, *221*, 103–115, doi:10.1016/S0012-821X(04)00070-6.

Replumaz, A., A. M. Negredo, S. Guillot, and A. Villaseñor (2010), Multiple episodes of continental subduction during India/Asia convergence: Insight from seismic tomography and tectonic reconstruction, *Tectonophysics*, *483*, 125–134, doi:10.1016/j.tecto.2009.10.007.

Ritzwoller, M. H., and A. L. Levshin (1998), Eurasian surface wave tomography: Group velocities, *J. Geophys. Res.*, *103*, 4839–4878, doi:10.1029/97JB02622.

Ritzwoller, M. H., M. P. Barmin, A. Villaseñor, A. L. Levshin, and E. R. Engdahl (2002a), Pn and Sn tomography across Eurasia, *Tectonophysics*, *358*(1–4), 39–55, doi:10.1016/S0040-1951(02)00416-X.

Ritzwoller, M. H., N. M. Shapiro, M. P. Barmin, and A. L. Levshin (2002b), Global surface wave diffraction tomography, *J. Geophys. Res.*, *107*(B12), 2335, doi:10.1029/2002JB001777.

Rodgers, A. J., W. R. Walter, R. J. Mellors, A. M. S. Al-Amri, and Y-S. Zhang (1999), Lithospheric structure of the Arabian shield and platform from complete regional waveform modeling and surface wave group velocities, *Geophys. J. Int.*, *138*, 871–878, doi:10.1046/j.1365-246x.1999.00918.x.

Roecker, S. W. (1982), Velocity structure of the Pamir–Hindu Kush region: Possible evidence of subducted crust, *J. Geophys. Res.*, *87*, 945–959.

Sahu, V. K., V. K. Gahalaut, S. Rajput, R. K. Chadha, S. S. Laishram, and A. Kumar (2006), Crustal deformation in the Indo-Burmese arc region: Implications from the Myanmar and southern Asia GPS measurments, *Curr. Sci.*, *90*, 1688–1692.

Sobolev, S. V., A. Y. Babeyko, I. Koulakov, and O. Oncken (2006), Mechanism of the Andean orogeny: Insight from the numerical modeling, in *The Andes: Active Subduction Orogeny*, *Frontiers in Earth Sciences*, vol. 1, edited by O. Oncken et al., pp. 513–535, Springer, New York.

Stöcklin, J. (1968), Structural history and tectonics of Iran: A review, *Am. Assoc. Pet. Geol. Bull.*, *52*(7), 1229–1258.

Takin, M. (1972), Iranian geology and continental drift in the Middle East, *Nature*, *235*, 147–150, doi:10.1038/235147a0.

van der Sluis, A., and H. A. van der Vorst (1987), Numerical solution of large, sparse linear algebraic systems arising from tomographic problems, in *Seismic Tomography*, edited by G. Nolet, pp. 49–83, Reidel, Dortrecht, Netherlands.

van der Voo, R., W. Spakman, and H. Bijwaard (1999), Tethyan subducted slabs under India, *Earth Planet. Sci. Lett.*, *171*, 7–20.

Verdel, C., B. P. Wernicke, J. Ramezani, J. Hassanzedeh, P. R. Renne, and T. L. Spell (2007), Geology and thermochronology of Tertiary Cordilleran-style metamorphic core complexes in the Saghand region of central Iran, *Geol. Soc. Am. Bull.*, *119*(7/8), 961–977, doi:10.1130/B26102.1.

Vernant, P., et al. (2004), Present day crustal deformation and plate kinematics in the Middle East constrained by GPS measurements in Iran and northern Oman, *Geophys. J. Int.*, *157*(1), 381–398, doi:10.1111/j.1365-246X.2004.02222.x.

Villaseñor, A., M. Ritzwoller, A. Levshin, M. Barmin, E. Engdahl, W. Spakman, and J. Trampert (2001), Shear velocity structure of central Eurasia from inversion of surface wave velocities, *Phys. Earth Planet. Inter.*, *123*, 169–184, doi:10.1016/S0031-9201(00)00208-9.

Vinnik, L. P., A. A. Lukk, and I. L. Nersesov (1977), Nature of the intermediate seismic zone in the mantle of the Pamir-Hindu Kush, *Tectonophysics*, *38*, 9–14.

Vinnik, L. P., C. Reigber, I. M. Aleshin, G. L. Kosarev, M. K. Kaban, S. I. Oreshin, and S. W. Roecker (2004), Receiver function tomography of the central Tien Shan, *Earth Planet. Sci. Lett.*, *225*, 131–146, doi:10.1016/j.epsl.2004.05.039.

Wu, F. T., A. L. Levshin, and V. M. Kozhevnikov (1997), Rayleigh wave group velocity tomography of Siberia, China and the vicinity, *Pure Appl. Geophys.*, *149*, 447–473, doi:10.1007/s000240050035.

Zhiwei, L., S. Roecker, Zhihai Li, Wei Bin, Wang Haitao, G. Schelochkov, and V. Bragin (2009), Tomographic image of the crust and upper mantle beneath the western Tien Shan from the MANAS broadband deployment: Possible evidence for lithospheric delamination, *Tectonophysics*, *477*, 49–57, doi:10.1016/j.tecto.2009.05.007.

Zonenshain, L. P., and L. Savostin (1981), Geodynamics of the Baikal rift zone and plate tectonics of Asia, *Tectonophysics*, *76*, 1–45, doi:10.1016/0040-1951(81)90251-1.

I. Koulakov, Institute of Petroleum Geology and Geophysics, SB RAS, Prospekt Akademika Koptuga, 3, Novosibirsk, 630090, Russia. (koulakoviy@ipgg.nsc.ru)